Journal of Natural Gas Science and Engineering 28 (2016) 280–304

Contents lists available at ScienceDirect

Journal of Natural Gas Science and Engineering

journal homepage: www.elsevier.com/locate/jngse

A fully coupled thermal-hydrological-mechanical-chemical model for CO_2 geological sequestration[☆]

Ronglei Zhang[*], Xiaolong Yin, Philip H. Winterfeld, Yu-Shu Wu

Energy Modeling Group, Petroleum Engineering Department, Colorado School of Mines, United States

A R T I C L E I N F O

Article history:
Received 20 September 2015
Received in revised form
15 November 2015
Accepted 17 November 2015
Available online 26 November 2015

Keywords:
THMC processes
Fully coupled method
CO_2 Geo-sequestration
Numerical simulation
Non-isothermal reactive transport
Mean stress
MC coupling
TH coupling
HM coupling

A B S T R A C T

The importance of thermal-hydrological-mechanical-chemical (THMC) interactions is well recognized in the procedure of CO_2 geo-sequestration. Geo-mechanics and geo-chemistry may have significant effects on the aqueous phase composition, porosity and permeability of the formation, which in turn affect flow and transport processes. Using a mean stress formulation, geomechanical effects are considered such as stresses, displacements, and rock deformation in CO_2 sequestration. Chemical equilibrium and kinetics are taken into account in the mass balance equation, which is able to quantitatively simulate fluid flow, solute transport and geo–chemical reaction in the operation of CO_2 geo-sequestration. Since rock strength decreases with increasing amounts of reactive minerals, substantial dissolution/precipitation of rock composition may lead to significant changes in the mechanical behavior, a generic computational scheme has been developed to take the mechanical and chemical coupling effects into account. Based on these theories, a novel mathematical model of the THMC processes is developed in this paper. A fully coupled computational framework is proposed and used to simulate reactive transport of water, CO_2 gas and species in subsurface formation with geomechanics. The novel frameworks are designed to keep a generalized computational structure for different THMC processes. The coupled THMC simulators focus on: (1) fluid and heat flow, solute transport in a three-phase mixture, (2) stress and displacement related to mean stress, (3) non-isothermal effects on fluid properties and reaction processes, and (4) the equilibrium and kinetics of water-rock and gas-rock chemical interactions. A practical reactive transport examples with cold supercritical CO_2 injection into saline aquifer has been proposed to analyze the THMC processes quantitatively. It is indicated that the geochemical reactions do not have significant impact on pore pressure, mean stress and temperature. The thermal energy transport with low temperature significantly affects the mean stress and geochemical reactions in the saline aquifer. Low temperature accelerates equilibrium dissolution of gas and mineral, but slows down kinetic dissolution/precipitation of minerals, such as anorthite and kaolinite.

1. Introduction

Based on the technical report of Intergovernmental Panel on Climate Change (IPPC), the concentration of CO_2 in the air has been increased by one third over the past 150 years, and is currently still rising by about 1.7 ppmv every year (IPCC, 2007). While CO_2 reacting with the molecules of water in the atmosphere, soil and ocean system, carbonic acid and hydrogen ions are formed, leading to an acidized environment. The ecosystems in the ocean are influenced by aqueous acidification and the concentration reductions of associated carbonate ion (Orr et al., 2005). Only 25% of CO_2 emissions to the atmosphere by human activities can be absorbed and utilized by the terrestrial biosphere (Feely et al., 2004), thus CO_2 emissions have significant effects on the environment. Therefore, CO_2 geo-sequestration into saline aquifers is the most effective solution to reduce CO_2 emissions. Saline aquifers have the largest volumetric capacity among the many options for long term geological storage of CO_2 (IPCC, 2005). The sketch of CO_2 geo-sequestration is shown in Fig. 1. After a large amount of CO_2 is injected into the aquifers, there are several primary mechanisms controlling the percolation and ultimate fate of CO_2(IPCC, 2005). The effectiveness of geological storage depends on a combination of the trapping mechanisms (IPCC, 2005):

[☆] Fully documented templates are available in the elsarticle package on CTAN.

[*] Corresponding author.

E-mail address: zhangronglei@gmail.com (R. Zhang).

http://dx.doi.org/10.1016/j.jngse.2015.11.037
1875-5100/© 2015 Elsevier B.V. All rights reserved.

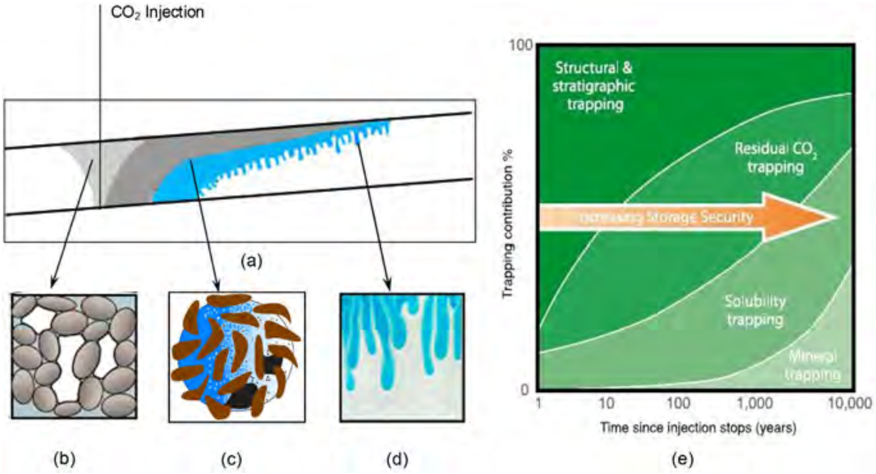

Fig. 1. The Sketch for trapping mechanism during CO_2 geo-sequestration: (a) Structural Trapping; (b) Residual Trapping (Szulczewski et al., 2012); (c) Mineral Trapping; (d) Solubility Trapping (Szulczewski et al., 2012); (e) Trapping Contribution (IPCC, 2005).

Stratigraphic and structural trapping. The physical trapping of gaseous CO_2 below cap-rocks and above bed-rock, such as shale or clay seals with ultra low permeabilities, is the primary means to sequestrate gaseous CO_2 in geological reservoirs (Yao et al., 2012; Zhang et al., 2014). Fig. 1 (a) shows that CO_2 injected in the saline aquifer can be sealed between the cap rock and the bed rock. Both the free CO_2 gas phase and two phase mixture are trapped in this manner. Such stratigraphic traps are often located in sedimentary basins, and are occupied by saline water, oil and gas. Structural trapping are resulted from the variations of rock types caused by changes in the way the sediments were deposited. In addition, CO_2 can be trapped in the pore space by capillary forces and relative permeability, which is shown in Fig. 1 (b).

Solubility trapping. It occurs in the saline aquifers where fluids transport very slowly over long distances. After CO_2 is injected into the aquifer, it displaces aqueous water and migrates upwards. Under the formation pressure, gaseous CO_2 becomes equilibrated with formation water, leading to aqueous CO_2 in the formation water. Dispersion and fingering of aqueous CO_2 may be formed due to permeability heterogeneity, gravity override and mobility contrast between CO_2 and formation fluid, which is shown in Fig. 1 (d). These mechanisms also operate over relatively short timescales (injection period).

Mineral trapping. After CO_2 is dissolved into formation water, carbonic acid is released to dissolve certain amount of rock minerals, leading to a decrease of the pH value. Dissolved ions and minerals may further react to form stable carbonate and silicate minerals. The interaction between CO_2 and water is shown in Fig. 1 (c). Reaction of dissolved CO_2 with minerals can be very rapid (days) for some carbonate minerals, but very slow (hundreds to thousands of years) for others (silicate minerals). This mechanism operates over long timescales (thousand years) and relatively small site scale (formation scale).

The trapping contributions for the CO_2 mass that can be trapped by the different mechanisms are show in Fig. 1 (e) schematically. The extent of the contribution is in the order of structural and residual trapping, solubility and mineral trapping.

1.1. Description for THMC processes

The physical mechanisms of CO_2 geo-sequestration discussed above is a thermal-hydrological-mechanical-chemical processes. The trapping mechanism is in the macroscopic perspective, however it is resulted from the change in the pore structure subjected to supercritical CO_2 injection. The THMC processes due to supercritical CO_2 injection in the perspective of pore structure are described as follows: (a) The original pore structure in the saline aquifer is under hydrostatic equilibrium with water and a small amount of non-aqueous liquid phase (NAPL) saturated in the small pores. The chemistry between water, NAPL and mineral is in equilibrium condition. There is a small amount of mineral dissolved into the aquifer water, resulting in salinity at the original state of the aquifer. The phase between water and NAPL is also in equilibrium, a small amount of NAPL is dissolved in the water phase and the same with water in the NAPL phase. Fig. 2 (a) illustrates the original pore structure in the target saline aquifer for CO_2 geo-sequestration; (b) The pore structure is shrunk due to pressure buildup at the beginning of the CO_2 injection, especially the volume of the rock matrix tends to decrease. Fig. 2 (b) illustrates the shrunk rock matrix and the enlarged pore space due after CO_2 injection; (c) The pore structure is changed due to large amount of supercritical CO_2 injection in a short period, in the perspective of pore compressibility and thermal expansivity. When the CO_2 gas (in blue color as in Fig. 2 (c)) is squeezed into the pore space, the pressure and stress in the target aquifer increase greatly. The rock matrix tends to shrink under great pore pressure and stress, which result in the increase of space in the pore structure. The porosity and permeability of the formation increase due to the pore space increase. Fig. 2 (c) illustrates that the pore space increases by a large amount of CO_2 injection; (d) The phase is equilibrated between saline water and gas simultaneously after CO_2 injection into the saline aquifer. In the perspective of phase equilibrium, the saline water is evaporated into the gaseous CO_2 phase (H_2O (aq) = H_2O (gas)), and the gaseous CO_2 is dissolved into aquifer water (CO_2(gas) = CO_2(aq)). Both processes are under high pressure and high temperature. As you may see in Fig. 2 (d), the molecules of CO_2(aq) (compounds with blue color in aquifer water) are distributed into the aquifer water gradually, and small molecules of H_2O (compounds with white color in gaseous CO_2 phase) is trapped in the gaseous CO_2 phase; (e) The pH value is evolved due to dissolution of gaseous CO_2 in aquifer water. In the perspective of chemical reaction, the gaseous CO_2 is dissolved into aquifer water (CO_2(gas) = CO_2(aq)). The large amount of chemical species CO_2(aq) releases into aquifer water, when the phases achieve equilibrium state. Then, CO_2(aq)

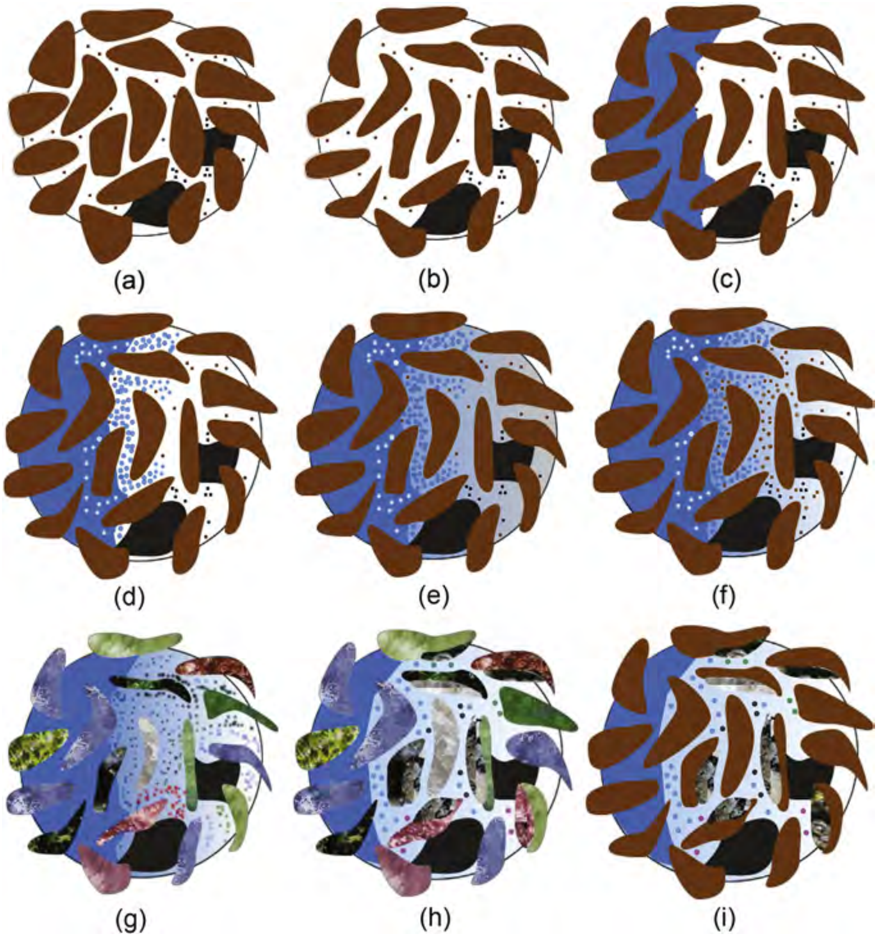

Fig. 2. Sketch for THMC processes during CO_2 injection into the saline aquifer in the perspective of pore structure: (a) original pore structure under hydrostatic equilibrium; (b) shrunk pore structure under fluid injection; (c) pore structure after CO_2 injection of short period; (d) phase re-equilibrium between water and gas after CO_2 injection; (e) pH value evolution due to solubility of gaseous CO_2; (f) aquifer salinity evolution due to pH change in a relatively long period; (g) mineral dissolution due to acidized environment in a long period; (h) mineral precipitation due to interacting of different species in a very long period; (i) pore structure evolution due to mineral evolution in thousands of years.

reacts with H_2O molecules ($CO_2(aq) + H_2O = H^+ + HCO_3^-$) forming H^+ and HCO_3^-. Because of more independent H^+ releasing into the saline aquifer, the environment become acidized with a low pH value. As you may see in Fig. 2 (e), the pH value become lower as the color of water near the phase contact surface become darker; (f) The salinity in the aquifer increases due to the change of pH value in a relatively long period. The pH value become lower with CO_2(gas) dissolves into aquifer water. The independent H^+ is more than sufficient in the aquifer water, which leads to the dissolution of rock minerals. The carbonate minerals tend to be dissolved rapidly in an acidized environment. A large amount of ions (Fe^{2+}, Fe^{3+}, Mg^{2+}, Al^{3+}, Si^{4+} and Ca^{2+}, etc.) release into aquifer water, then the salinity of aquifer increase to a certain level. As you may in Fig. 2 (f), a large amount of chemical species dissolve into the aqueous phase from the rock matrix; (g) The rock mineral continues to be dissolved due to the acidized environment in a long period. There are different types of rock minerals in different saline aquifers. Most target saline aquifers in North America are in sandstone formations, and the common rock minerals are feldspar, clay, smectite, oligoclase, dolomite, calcite, illite, etc. The colors of rocks are changed to represent the different kinds of rock minerals in Fig. 2 (g). Within a long period after CO_2 injection, the mass and volume of rock minerals become decreased and shrunk due to the dissolution of the minerals. A certain amount of H^+ has been consumed due to the dissolution of rock minerals. This is a process of pH buffering, and the pH value tends to increase to be above 7. The porosity and permeability in the pore structure tend to increase, see Fig. 2 (g) and 2 (h). The minerals are precipitated due to interacting of different chemical species in a very long period. After the dissolution of rock minerals and CO_2 gas, different chemical species precipitate new rock minerals, especially carbonate mineral and silicate minerals (siderite, dolomite, calcite, quartz, illite, ankerite, dawsonite, etc.). The newly precipitated rock minerals is coated on the surface of the shrunk original rock minerals, which resulting in a decrease of porosity and permeability of the saline aquifer. As you may see in Fig. 2 (h), the pore space is reduced due to the precipitation of newly generated rock minerals, and pH value continues to increase due to the consumption of H^+ (the color of the aquifer water become lighter); (i) The pore structure evolution due to mineral evolution in thousands of years. Fig. 2 (i) shows that the rock minerals newly precipitated on the surface of the aquifer rocks, which extend into the pore spaces, causing a decrease of porosity and permeability. The saturation of supercritical CO_2 decreased due to mineralization of CO_2 in solid phase. The pore structure has been changed significantly as shown in the figure. As mechanical behavior is closely related to the petrophysical properties of the rock material, supercritical CO_2 induced chemical changes may lead to significant mechanical weakening in porous and permeable saline aquifer. Rock strength increases with increasing content of strong/hard minerals (e.g. quartz, feldspar), and decreases with increasing amounts of weak/soft minerals (e.g.clay, mica) and porosity. Few studies has concluded that in the case of substantial dissolution/precipitation of framework grains or framework-supporting cements, significant changes in the mechanical behavior are to be expected, and the elastic parameters are proportional to the rock compositions (Marbler et al., 2013; Busch et al., 2014; Hangx et al., 2015). The lack of a simple correlation and a clear computational scheme between rock elastic parameters and rock strength suggests that more experimental studies needs to be conducted. However, We proposed a generic computational scheme to take the mechanical and chemical coupling effects in the numerical model.

1.2. *Chemical reaction pathway*

The chemical reaction pathway depends upon rock compositions. According to the mineral compositions of the CO_2 geo-sequestration sites, the most common formations are categorized into three kinds: sandstone, carbonate and clay. In terms of the rock type, the rock minerals in these three formations are quite similar, but the volume fractions of the rock minerals vary significantly. These formations are always composed of quartz, carbonate minerals, plagioclase feldspar minerals, clay minerals, and minor other components. Calcite represents the carbonate minerals. Oligolcase and K-feldspar represent the plagioclase feldspar minerals. Clay minerals includes kaolin group (kaolinite), illite group (illite), smectite group (smectite-Na and smectite-Ca) and chlorite group (chlorite). Furthermore, the chemical reaction pathway after supercritical CO_2 injection can be described in terms of rates of the kinetic reactions. Based on the parameters of the kinetic rates given by Xu et al., 2006, the kinetic reactions rates are small and vary significantly for different rock minerals. Carbonate minerals have the fastest kinetic reaction rates (in the magnitude of 10^{-7} mol/m^2 s), then plagioclase feldspar minerals have the kinetic reaction rates in the magnitude of 10^{-12} mol/m^2 s, illite minerals and smectite minerals have the kinetic reaction rates in the magnitude of 10^{-13} mol/m^2 s, kaolin minerals and quartz have the kinetic reaction rates in the magnitude of 10^{-14} mol/m^2 s. The kinetic chemical reaction rates are also related to the reactive surface area of rock, the acid or base mechanism involved in the aqueous phase, the activation energy and temperature.

In terms of the rock mineral compositions and kinetic rates, the chemical reaction pathway can be described in Fig. 3. Every small pore can be treated as a batch reactor when supercritical CO_2 invades into it. The CO_2 dissolution is the fastest chemical reaction, the chemical equilibrium of CO_2 dissolution is reached simultaneously with the injection of supercritical CO_2. It releases large amounts of hydrogen ion, leading to an acidized aqueous environment. This process is an acidized process. Secondly, the carbonate minerals such as calcite, dolomite, magnesite start to dissolve into the aqueous phase. Various iron species and bicarbonate species are releasing into the aqueous phase. The rates of the carbonate mineral dissolution are in the magnitude of 10^{-7} mol/m^2 s, and the dissolution of carbonate minerals reaches the equilibrium state rapidly. Thirdly, the rock minerals from plagioclase group, kaolin group, illite group, smectite group and chlorite group starts to dissolve into the aqueous phase under the effects of chemical species H^+. This process is defined as pH buffering. The minerals break into large amounts of different chemical species in aqueous phase. K-feldspar and chlorite are taken as examples to illustrate how the minerals dissociate into different chemical species in Fig. 3. It may take thousands of years for the minerals dissolutions. These three processes are dissolutions of gas and minerals. After this, the new minerals precipitate into the solid phase on the surface of the formation. The new minerals are mainly composed of stable carbonate mineral such as dawsonite, ankerite and siderite. The precipitation of the new minerals are relatively fast in the magnitude of 10^{-8} mol/m^2 s after the mineral dissolution. Finally, the slowest reaction is the precipitation of quartz in the magnitude of 10^{-14} mol/m^2 s. The last two processes lead to the mineral trapping of supercritical CO_2 in solid phase, and continue to buffer pH value and consume the chemical species of H^+. Based on the analysis above, the chemical reaction pathway of supercritical CO_2 with rock minerals is complicated due to the key factors (rock type, rock composition, reaction rate, etc.)

1.3. *Numerical simulation scheme and algorithm for THMC processes*

For the numerical simulations of the THMC processes, THM processes and THC processes are always coupled separately to solve different problems in both systems. Among many factors of the THMC processes to be considered in the numerical models, the geomechanical effects take place immediately after the working fluid injection, leading to pore structure change and land subsidence. The geochemical reactions that take place between injected CO_2, water and the rock minerals are much more complex. It is a challenging issue to model the THMC processes within a coupled

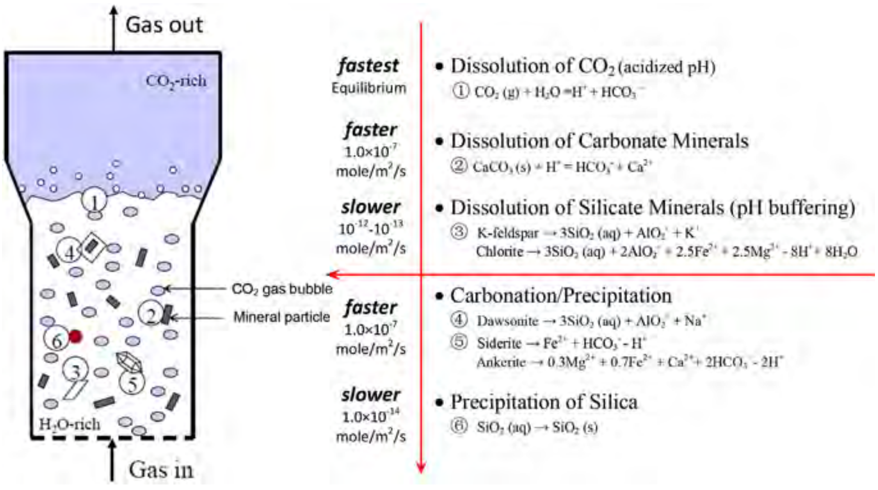

Fig. 3. The sketch for the chemical reaction pathway in the THMC processes during CO_2 geo-sequestration.

procedure mathematically, because of the complexity of multiphase fluid and heat flow, geomechanics, geochemical reactions of water-gas-rock, and the strong non-linearities in the mass, energy and momentum conservation equations. Among the four processes, THM processes and THC processes are always coupled separately to solve for CO_2 geo-sequestration, but these coupled processes don't have capabilities to address the mutual effects of thermal gradients, geomechanics and geochemistry quantitatively. It is necessary for us to develop a THMC model. There are few numerical studies to couple the THMC processes together. Among the THMC processes, the THC process is much more complex than THM. Many numerical studies have addressed the coupled methods for THC processes. The numerical scheme and algorithm for THMC processes can be based on that of THC processes. There are two major methods widely used to solve the THC processes, i.e. sequentially coupled approach and fully coupled approach. The first one solves the fluid transport and the geochemistry individually and sequentially in an iterative manner (Cederberg et al., 1985; Yeh and Tripathi, 1991; Engesgaard and Kipp, 1992; Šimnek and Suarez, 1994; Walter et al., 1994; Zysset et al., 1994; Xu, 1996; Wei, 2012; Zhang et al., 2015). Furthermore, a modified sequential noniterative approach was proposed to solve solute transport and chemistry only once without iteration (Liu and Narasimhan, 1989; Ague and Brimhall, 1989; Appelo, 1994). By means of sequential iteration approach, a set of geochemical codes such as SOLMINEQ (Kharaka et al., 1989), EQ3/6 (Wolery, 1992), PHREEQE (Parkhurst et al., 1991), PATHARC (Hitchon, 1996), PHREEQC V2.0 (Parkhurst et al., 1999), GEOCHEMIST'S WORKBENCH (Bethke, 2002), TOUGHREACT (Xu et al., 1997), and UTCHEM (Delshad et al., 1996; Najafabadi et al., 2009) are designed to couple the fluid flow, solute transport, and geochemical reaction sequentially. Among them, TOUGHREACT are developed to solve the multi-dimensional and multi-phase fluid flow, solute transport, and chemical reactions in groundwater and petroleum systems, respectively. There are few studies of the fully coupled approach (Guimarães et al., 2007; Zheng and Samper, 2008; Zhang et al., 2012a, b; Xiong et al., 2013; Zhang, 2013; Wu et al., 2014; Zheng et al., 2015), it substitutes the geochemical reaction into the fluid flow equations directly, forming a fully coupled reactive solute transport model. This approach solves the fluid flow, solute transport, and geochemical reactions simultaneously with a high accuracy. Therefore, we use the fully coupled approach to solve the THC processes together, in order to get accurate solutions.

There are many developments for the algorithm of THM models (Settari et al., 2001; Longuemare et al., 2002; Minkoff et al., 2003; Tran et al., 2004; Samier et al., 2008; Zhao et al., 2015a, b). The procedures of coupling algorithm can be categorized into three kinds: loosely coupled, iteratively coupled and fully coupled. Basically, there are two sets of equations (heat and fluid flow, geomechanics) to be solved in the algorithm. The loosely coupled method solves the geomechanics after a certain number of time steps of fluid flow. A certain amount of THM simulators employ the loosely coupled procedure to solve fluid flow and geomechanics, e.g., TOUGH-FLAC (Rutqvist and Tsang, 2002; Rutqvist et al., 2002), ATH2VIS (Longuemare et al., 2002), and IPARS-JAS3D (Minkoff et al., 2003). Secondly, the iteratively coupled procedure solves the primary variables for heat and fluid flow, and primary variables for geomechanics individually and sequentially. The solutions are delivered into equations of heat, fluid flow and geomechanics back and forth in both directions at a specific time point. Then the THM procedures are coupled iteratively at the end of each time step (Longuemare et al., 2002). In this procedure, either the equations of heat and fluid flow or the equations of geomechanics are solved initially, and then the other equations can be solved sequentially and iteratively by substituting the intermediate solutions, e.g., GEOSIM (Settari et al., 2001), Rocflow (Wang and Kolditz, 2007). A typical example of this iteratively coupled method is explicitly coupled method. It only allows one iteration per one time step, e.g., ROCMAS (Noorishad et al., 1984), FRACture (Kohl et al., 1995) and FRACON (Nguyen, 1996). Furthermore, the fully coupled procedure solves a set of nonlinear partial differential equations, which represents all the related physical mechanisms (Minkoff et al., 2003). Thus, the equations of heat flow, fluid flow and geomechanics are solved simultaneously at each time step. TOUGH_CSM (Winterfeld and Wu, 2012) is a successful implementation of fully coupled procedure, which solves the fluid flow and mean stress equation simultaneously.

In this paper, a fully coupled computational framework is proposed and used to simulate reactive transport of water, CO_2 gas and species in subsurface formation with geomechanics. A novel mathematical model of the THMC processes is developed based on the TOUGHREACT simulator (Xu et al., 2004) and TOUGH2_CSM simulator (Winterfeld and Wu, 2012). A set of partial differential equations is presented to model the THMC processes of the fluid and heat flow, solute transport in aqueous and gaseous phase, mean stress, and geochemical reactions under both equilibrium and kinetic conditions. Practical reactive transport examples with complex chemical compositions are presented to analyze the THMC processes quantitatively on the coupled effects of geochemical reaction and geomechanics during CO_2 geo-sequestration process. Heat transfer affects mean stress and geochemical reactions, mean stress impacts the solute transport and successive chemical reactions. The proposed modeling approach can also be used to simulate CO_2 EOR and other secondary and EOR processes in petroleum reservoirs.

2. Mathematical model

The THMC processes are described mathematically, including mass balance equation to describe the fluid flow and mass transport, momentum balance equation to describe the mean stress field, energy balance equation to describe the heat flow and energy transport, and geochemical reaction equation to describe the geochemistry occurring during CO_2 geo-sequestration. Geo-chemical equilibrium and kinetics equations are based on TOUGHREACT simulator (Xu et al., 2006), and mean stress equation is based on TOUGH_ CSM simulator (Winterfeld and Wu, 2012). The assumptions and the mathematical formulations of the THMC model are shown as below.

2.1. Assumptions

The THMC model is developed for multi-dimensional porous media with heterogeneous physical and chemical properties. The gaseous, aqueous and solid phases are involved in heat flow, fluid flow, geomechanics and geochemical reactions. The effects of heat, pressure and stress are taken into account for the calculation of physical, geomechanical and geochemical properties. Multiphase Darcy flow formulation is applied for the fluid flow in porous media. A simplified mean stress formulation is used in this THMC model. Transport of aqueous and gaseous species by advection is taken into account. Any kind of chemical species in liquid, gas, and solid phases can be simulated in this model. Thermodynamic equilibrium are considered between gaseous species and the corresponding aqueous species. Aqueous complexation and gas dissolution are considered under the local equilibrium assumption. Thermodynamic and chemical equilibrium are attained instantly within each grid cell. Mineral dissolution and precipitation predefined in the model can occur either under local equilibrium or kinetic conditions. The porosity is subject to the mutual change of stress and chemical reactions under the coupling effects of HM and

HC. The geomechanical modulus is subject to the change of chemical compositions of the porous medium under the coupling effect of MC. The contigential TH effects such as thermal osmosis are not taken into account in the model.

2.2. Mass conservation equation

In the sequentially coupled procedure, the first part only solve the mass balance for a certain number of primary components (i.e., H_2O, NaCl, and CO_2), mass loss or gain of primary components in chemical reactions are considered in the equation. The mass balance for primary components κ in accordance to Darcy's law can be written in the following form:

$$\frac{dM^{\kappa}}{dt} = \nabla \cdot F^{\kappa} + q^{\kappa} + R^{\kappa} \tag{1}$$

The quantity M is the accumulation term, representing mass of a primary components or species, with $\kappa = 1, \ldots, N_k$ κ is the primary components or species (H_2O, NaCl, and CO_2). F is the mass flux based on the Darcy's Law, and q is sinks and sources of primary components. R denotes mass or loss for H_2O and CO_2 due to chemical reactions, which are the feedbacks from the third part of geochemical reaction module.

The general form of the mass accumulation term is

$$M^{\kappa} = \phi \sum_{\beta} S_{\beta}\rho_{\beta}X_{\beta}^{\kappa} \tag{2}$$

The total mass of primary component or species κ is obtained by summing over the fluid phases β (= water and gas). ϕ is porosity, S_{β} is the saturation of phase β, ρ_{β} is the density of phase β, X_{β}^{κ} is the total mass fraction of primary component or chemical species κ in phase β, and X_{β}^{κ} is the function of the concentration of related primary chemical species $c_{p,j}$, i.e., $X_{\beta}^{\kappa} = f(c_{p,j})$.

Total mass fraction of primary chemical species.

In order To represent the whole geochemical system, a set of N_C aqueous species is chosen as primary species or components. All the other species are treated as secondary species, including aqueous complexes, precipitated minerals and gaseous species. The secondary species can be represented as a linear combination of the associated primary species. Therefore, all the mass of the secondary species can be transferred to the mass of primary chemical species. The total concentration of primary species can be expressed as:

$$C_j = c_j + \sum_{k=1}^{N_x} \nu_{kj}c_k \quad j = 1, \ldots, N_C \tag{3}$$

where C and c are the total concentrations and individual concentrations; subscripts j and k are the indices of primary species and aqueous complexes; N_C and N_x are the number of the primary and secondary species; ν_{kj} is the stoichiometric coefficient of the basis species in the aqueous complexes.

The total mass fraction of the primary chemical species can be defined as:

$$X^{\kappa} = \frac{C^{\kappa}M^{\kappa}}{\rho_l} \quad \kappa = 1, \ldots, N_C \tag{4}$$

where M^{κ} is the molecular weight of the primary chemical species, and ρ_l is the density of the aqueous phase.

Aqueous complexation

The aqueous chemical reactions are always under local equilibrium. By means of the mass action equation of the dissociation of the i-th aqueous complex, the concentrations of aqueous complexes can be represented as functions of the concentrations of primary species:

$$c_k = K_k^{-1}\gamma_k^{-1}\prod_{j=1}^{N_c} c_j^{\nu_{kj}}\gamma_j^{\nu_{kj}} \tag{5}$$

where c_k is the molal concentration of k-th secondary aqueous complexation, and c_j is molal concentration of the jth basis species, γ_k and γ_j are thermodynamic activity coefficients of secondary and primary species, and K_k is the equilibrium constant of the k-th secondary complexation reaction.

Kinetic mineral dissolution/precipitation

The expression of kinetic rate is given by Lasaga et al. (1994):

$$r_n = f(c_1, c_2, \ldots, c_{N_C}) = \pm K_n A_n\left|1 - \Omega_n^{\theta}\right|^{\eta} \quad n = 1, \ldots, N_q \tag{6}$$

where A_n is the specific reactive surface area, Ω_n is the saturation ratio of kinetic mineral, the definition of saturation ratio is explained later. The parameters θ and η are assumed to be one. The values of r_n could be positive and negative, which denote dissolution and precipitation of corresponding mineral respectively. k_n is the rate constant, which is a temperature dependent variable. It is expressed by an Arrhenius equation (Lasaga, 1984; Steefel and Lasaga, 1994). In terms of the different chemistry mechanism, dissolution and precipitation of minerals are not only catalyzed by pure H_2O (neutral mechanism), but also by H^+ (acid mechanism) and OH^- (base mechanism). The equation of K_n in terms of the three mechanisms can be expressed by (Lasaga et al., 1994; Palandri and Kharaka, 2004):

$$\begin{aligned} k_n = {} & k_{25}^{\mathrm{n}}\exp\left[\frac{-E_{\mathrm{a}}^{\mathrm{n}}}{R}\left(\frac{1}{T} - \frac{1}{298.15}\right)\right] \\ & + k_{25}^{\mathrm{H}^+}\exp\left[\frac{-E_{\mathrm{a}}^{\mathrm{H}^+}}{R}\left(\frac{1}{T} - \frac{1}{298.15}\right)\right]a_{\mathrm{H}^+}^{n_{\mathrm{H}^+}} \\ & + k_{25}^{\mathrm{OH}^-}\exp\left[\frac{-E_{\mathrm{a}}^{\mathrm{OH}^-}}{R}\left(\frac{1}{T} - \frac{1}{298.15}\right)\right]a_{\mathrm{OH}^-}^{n_{\mathrm{OH}^-}} \end{aligned} \tag{7}$$

where E_a is the activation energy, k_{25} is the rate constant at 25° C, R is gas constant, T is absolute temperature, $a_{\mathrm{H}^+}^{n_{\mathrm{H}^+}}$ is the activity of H^+, which is the product of activity coefficient (γ_{H^+}) and concentration of H^+ (c_{H^+}), and $a_{\mathrm{OH}^-}^{n_{\mathrm{OH}^-}}$ is the activity of OH^-, which is the product of activity coefficient (γ_{OH^-}) and concentration of OH^- (c_{OH^-}).

2.3. Energy conservation equation

The energy balance equation is derived under the assumptions that energy is a function of temperature only and energy flux in the porous media occurs by advection and heat conduction only.

$$\frac{dU}{dt} = \nabla \cdot F + q_{\mathrm{h}} \tag{8}$$

where U is the heat accumulation term of rock and fluid, F_{β} is the heat flux, and q_h is the heat sink and source by heat injection and withdraw.

2.4. Geomechanical equation of mean stress

The mean stress equation in this THMC model is based on the equation by Winterfeld et al. (2012), which is to solve the normal mean stress. The mean stress equation is given below.

$$\frac{3(1-v)}{1+v}\nabla^2\tau_m - \frac{2(1-2v)}{1+v}\left(\alpha\nabla^2 p + 3\beta K\nabla^2 T\right) + \nabla\cdot\overline{F} = 0 \tag{9}$$

where v is the Poisson's ratio, τ_m is the normal mean stress, α is the Biot's coefficient, p is the pore pressure, β is the linear thermal expansion coefficient, K is the bulk modulus, F is body force, λ is the Lame's constant, G is the shear modulus, T is the temperature, and subscript $_m$ is the label of mean stress.

The geomechanical properties are expected to be correlated with the chemical compositions in the formation in a certain way, we proposed a generic computational scheme to incorporate the MC coupling effect into the numerical model. The geomechanical moduli is proportional to the rock compositions as follows:

$$K = K(c_1, c_2, \ldots, c_j) j = 1, \ldots, N_C + N_p + N_g \tag{10}$$

$$G = G(c_1, c_2, \ldots, c_j) j = 1, \ldots, N_C + N_p + N_g \tag{11}$$

where c_j is primary variable in the numerical model, then we can use the correlation between bulk modulus and shear modulus to calculate the other geomechanical properties in the model.

2.5. Geochemical reaction equations for gas at equilibrium condition

The chemical reactions between aqueous and gaseous species are set to be under a condition of local equilibrium. Based on the Mass Action Law, we obtain the following expression:

$$F_g = \log\Omega_g = \log\Gamma_g^{-1} p_g^{-1} K_g^{-1} \prod_{j=1}^{N_c} c_j^{v_{gj}} \gamma_j^{v_{gj}} = 0 \tag{12}$$

where subscript g represents gas index, p is the partial pressure of gaseous phase, Γ is the fugacity coefficient of gaseous species.

2.6. Geochemical reaction equations for mineral at equilibrium condition

In a geochemical reaction system, the dissolution rate of a certain mineral (i.e., $CaCO_3$) is very fast. The reaction of the mineral is always set to be at equilibrium, the mineral saturation index controls the dissolution of the mineral, and it can be expressed as:

$$F_m = \log\Omega_m = \log X_m^{-1} \lambda_m^{-1} K_m^{-1} \prod_{j=1}^{N_c} c_j^{v_{mj}} \gamma_j^{v_{mj}} = 0 \tag{13}$$

where m is the equilibrium mineral index, X_m is the mole fraction of the m^{th} mineral phase, λ_m is its thermodynamic activity coefficient, K_m is the corresponding equilibrium constant of the equilibrium mineral, C_j is the concentration of related primary chemical species or components, v_{mj} is the stoichiometric coefficient of j^{th} basis species in the m^{th} mineral equilibrium reaction, and γ_j is the activity coefficient of primary chemical species.

2.7. Porosity and permeability computational scheme for THMC coupling effects

The relationship between mean stress, τ_m, and porosity, ϕ, has been investigated extensively (Ostensen, 1986; McKee et al., 1988; Davies and Davies, 2001; Rutqvist and Tsang, 2002), which we have incorporated into our mechanical model formulation. We begin with mechanical changes in porosity as follows:

$$\phi_M = \phi(\tau'_m) \tag{14}$$

where subscript M indicates mechanical effects on porosity, τ'_m is the current effective mean stress as $\tau'_m = \tau_m - \alpha p$, and α is Biot coefficient,.

The chemical reaction model incorporates porosity changes due to mineral dissolution and precipitation as follows:

$$\phi_c = 1 - \sum_{m=1}^{N_m} f_m - f_u \tag{15}$$

where N_m is the number of reactive minerals, f_m is the total mineral fraction ($V_{mineral}/V_{medium}$), and f_u is the non-reactive fraction.

In the THMC processes, the porosity change within each time step $\Delta t = t^{k+1}$–t^k is given in terms of the changes in mechanical and chemical properties $\Delta\phi_M = \phi_M^{k+1} - \phi_M^k$ and $\Delta\phi_c = \phi_c^{k+1} - \phi_c^k$:

$$\phi^{t^{k+1}} = \phi^{t^k} + \Delta\phi_M + \Delta\phi_c \tag{16}$$

The permeability change is related to the porosity as follows:

$$k^{t^{k+1}} = k\left(\phi^{t^{k+1}}\right) \tag{17}$$

2.7.1. Porosity correlation

This THMC model is able to incorporate various correlations for stress-dependent porosity and permeability, but we can select an appropriate one for the specific filed.

1. Porosity Equation for sedimentary rock by Rutqvist and Tsang (2002).

Rutqvist and Tsang (2002) presented the following function for porosity, obtained from the laboratory experiment by Davies and Davies (2001) on sedimentary rock:

$$\phi = \phi_r + (\phi_0 - \phi_r)e^{-\alpha\tau'} \tag{18}$$

where ϕ_0 is zero effective stress porosity, ϕ_r is high effective stress porosity, the exponent a is a constant parameter, and τ' is effective mean stress.

2. Porosity Equation by McKee et al. (1988).

McKee et al. (1988) presented a relationship between porosity and effective stress from hydrostatic poroelasticity theory by assuming incompressible rock grains:

$$\phi = \phi_0 + \frac{e^{-c_p\left(\tau' - \tau'_0\right)}}{1 - \phi_0\left(1 - e^{-c_p\left(\tau' - \tau'_0\right)}\right)} \tag{19}$$

where c_p is the average pore compressibility, ϕ_0 is the original porosity, τ'_0 is the original effective mean stress, and τ' is the effective mean stress.

2.7.2. Permeability correlation

1. Permeability Equation by Bear (1972).

The changes of rock permeability are calculated from changes in porosity using ratios of permeabilities calculated from the Carman–Kozeny relation (Bear, 1972), and ignoring changes in grain size, tortuosity and specific surface area as follows:

$$k = k_o \left(\frac{1-\phi_o}{1-\phi}\right)^2 \left(\frac{\phi}{\phi_o}\right) \tag{20}$$

where k_o and ϕ_o are the initial permeability and porosity, respectively.

2. Permeability Equation for sedimentary rock by Rutqvist and Tsang (2002).

Another associated function for permeability in terms of porosity developed by Rutqvist and Tsang (Rutqvist and Tsang, 2002) is

$$k = k_0 e^{c\left(\frac{\phi}{\phi_0}-1\right)} \tag{21}$$

where k_0 is zero stress permeability and the exponent c is a parameter.

3. Permeability Equation by Verma and Pruess (1988).

Verma and Pruess (1988) presented a power law expression relating permeability to porosity as follows:

$$\frac{k-k_c}{k_0-k_c} = \left(\frac{\phi-\phi_c}{\phi_0-\phi_c}\right)^n \tag{22}$$

where k_c and ϕ_c are asymptotic values of permeability and porosity, respectively, and exponent n is a parameter.

4. Permeability Equation by Davies and Davies (2001).

One example from the study by Davies and Davies (2001) is given as follows:

$$k(\tau'_m) = k_i \frac{\left(1-\phi_i^2\right)^2}{(1-\phi_i)^2}\left(\frac{\phi}{\phi_i}\right)^3 \tag{23}$$

where ϕ_i is porosity at initial reservoir net stress, ϕ is porosity at reservoir net stress, $k(\tau'_m)$ is the permeability at net stress τ'_m and k_i is the permeability at initial reservoir net stress.

2.8. Discretization and solution method

The discretizations for mass conservation, energy conservation, mean stress and geochemistry equations have already been presented by Eqs. (1)–(13). For the fully coupled approach, the mathematical equations for fluid and heat flow, geomechanics, and geochemical reaction are solved simultaneously. Based on single cell, all the governing equations are lumped together in residual forms, and all the primary variable are defined as c_j. The discretized equation system can be expressed in residual forms as follows:

$$\begin{aligned} R_n^{\kappa,k+1} = {} & M_n^{\kappa,k+1} - M_n^{\kappa,k} - \frac{\Delta t}{V_n}\left[\sum_m A_{nm}F_{nm}^{\kappa,k+1} + V_n q_n^{\kappa,k+1}\right. \\ & \left. + V_n R_{\mathrm{req,n}}^{\kappa,k+1} + V_n R_{\mathrm{r,n}}^{\kappa,k+1}\right] \quad \kappa = 1,\ldots,N_C \end{aligned} \tag{24}$$

$$F_m^{k+1} = F_m\left(c_{j,k+1}\right) j = 1,\ldots,N_C + N_p + N_g \tag{25}$$

$$F_g^{k+1} = F_g\left(c_{j,k+1}\right) j = 1,\ldots,N_C + N_p + N_g \tag{26}$$

$$M^{k+1} = M\left(c_{j,k+1}\right) j = 1,\ldots,N_C + N_p + N_g \tag{27}$$

For each volume element V_n, there are N_{EQ} equations to describe the THMC processes. The total number of the non-linear equations representing the THMC system with N_{el} grid blocks is $N_{el} \times N_{eq}$. The unknown primary variables has the same number as the equations $c_j; j = 1, \ldots, N_{EL} \times N_{EQ}$, which define the state of the THMC system at a specific time step t^{k+l}. The method of Newton–Raphson iteration is employed to solve the equation system. A Newton–Raphson iteration index p is used to expand the residuals R at iteration step $p+1$ by means of Taylor series expansion. The Taylor series expansions of residual equations in terms of primary variables are as follows:

$$R_n^{\kappa,k+1}(c_{j,p+1}) = R_n^{\kappa,k+1}(c_{j,p}) + \sum_{j=1}^{N_C+N_p+N_g} \frac{\partial R_n^{\kappa,k+1}}{\partial c_j}\bigg|_p (c_{j,p+1} - c_{j,p}) \quad \kappa = 1,\ldots,N_C \tag{28}$$

$$F_m^{k+1}(c_{j,p+1}) = F_m^{k+1}(c_{j,p}) + \sum_{j=1}^{N_C+N_p+N_g} \frac{\partial F_m^{k+1}}{\partial c_{j,p}}\bigg|_p (c_{j,p+1} - c_{j,p}) \tag{29}$$

$$F_g^{k+1}(c_{j,p+1}) = F_g^{k+1}(c_{j,p}) + \sum_{j=1}^{N_C+N_p+N_g} \frac{\partial F_g^{k+1}}{\partial c_{j,p}}\bigg|_p (c_{j,p+1} - c_{j,p}) \tag{30}$$

$$M^{k+1}(c_{j,p+1}) = M^{k+1}(c_{j,p}) + \sum_{j=1}^{N_C+N_p+N_g} \frac{\partial M^{k+1}}{\partial c_{j,p}}\bigg|_p (c_{j,p+1} - c_{j,p}) \tag{31}$$

Retaining only terms up to first order, a set of $NEL \times NEQ$ linear equations for the increments ($c_{j,p+1}$-$c_{j,p}$) can be obtained as follows:

$$\sum_{j=1}^{N_C+N_p+N_g} \frac{\partial R_n^{\kappa,k+1}}{\partial c_j}\bigg|_p (c_{j,p+1} - c_{j,p}) = -R_n^{\kappa,k+1}(c_{j,p}) \quad \kappa = 1,\ldots,N_C + N_p + N_g \tag{32}$$

$$\sum_{j=1}^{N_C+N_p+N_g} \frac{\partial F_m^{k+1}}{\partial c_{j,p}}\bigg|_p (c_{j,p+1} - c_{j,p}) = -F_m^{k+1}(c_{j,p}) \tag{33}$$

$$\sum_{j=1}^{N_C+N_p+N_g} \frac{\partial F_g^{k+1}}{\partial c_{j,p}}\bigg|_p (c_{j,p+1} - c_{j,p}) = -F_g^{k+1}(c_{j,p}) \tag{34}$$

$$\sum_{j=1}^{N_C+N_p+N_g} \frac{\partial M^{k+1}}{\partial c_{j,p}}\bigg|_p (c_{j,p+1} - c_{j,p}) = -M^{k+1}(c_{j,p}) \tag{35}$$

For the fully coupled approach, the fluid flow and reactive solute transport equations are solved simultaneously until the prescribed convergence criteria are satisfied.

2.9. Convergence criteria

Referred to the Toughreact simulator (Xu et al., 2004), the convergence is achieved when the absolute value of the ratio between the relative increment of concentration and the concentration of primary components or species is less than a given convergence tolerance. The convergence criteria can be expressed as:

$$\frac{\left|\Delta c_{j,p+1}^{k+1}\right|}{c_{j,p}^{k+1}} \le \tau j = 1, 2, \cdots, N_c + N_p + N_g \tag{36}$$

where, τ is the convergence criterion.

2.10. Code structure of fully coupled THMC model

Fig. 4 shows the flow chart to solve the fully coupled THMC model. It solves the fluid and heat flow, geomechanics and geochemical reactions simultaneously in one time step. The governing equations for the geochemical reaction system interested are highly non-linear algebraic equations. They are solved by Newton–Raphson iteration method, and the matrix coefficients are calculated by the numerical derivatives related to the primary unknown variables.

3. Numerical modeling for THMC processes during CO_2 geological sequestration

The fully coupled THMC model is verified against different analytical solutions for the mechanisms involved in the THMC processes, including equilibrium chemical reaction, kinetic chemical reaction, heat conduction and geomechanical consolidation, and the numerical results have a good match with analytical solutions (Wu et al., 2014). In the THMC processes of CO_2 geo-sequestration, one mechanism may effect the others. The thermal effect influences the temperature, pressure, stress, and chemical reaction. High temperature can reduce the amount of gaseous CO_2 dissolved into aqueous phase, but may accelerate the chemical reaction, especially for mineral dissolution and precipitation pf rock minerals, and may increase the stress when subjected to CO_2 gas injection. In addition, the pressure increases subjected to CO_2 gas injection, which influence the phase equilibrium between CO_2 gas and aquifer water. This model is designed to show the mutual THMC effects during CO_2 geo-sequestration.

3.1. Hydrological and geomechanical Description

A 1D numerical model is subjected to large amount of CO_2 injection with low temperature. The model is assumed to be sealed by upper caprock and lower bedrock. A CO_2 injection well is located at the center of the radial system. The temperature of gaseous CO_2 is 32° C, which corresponds to the enthalpy of 5.632×10^5 J/kg and keep the gaseous CO_2 under supercritical condition (31.1° C and 7.4×10^6 Pa). The model is then discretized into 500 grid blocks in logarithmic distribution in the radial direction. The sandstone aquifer is assumed to be initially homogenous and isotropic in terms of hydrological and geological properties. The parameters of the model are given in Table 1. The initial condition of the temperature is set equal to 75° C in the model. For the boundary conditions, no-flow boundaries are assumed due to the impermeable seal layers along the top and bottom of this model. No-flow boundary conditions are assumed due to the radial symmetry of the CO_2 injection point at the left boundary. The constant boundary conditions of pressure and mean stress are assigned to the infinite radius of the simulation model at the right boundary. It is assumed

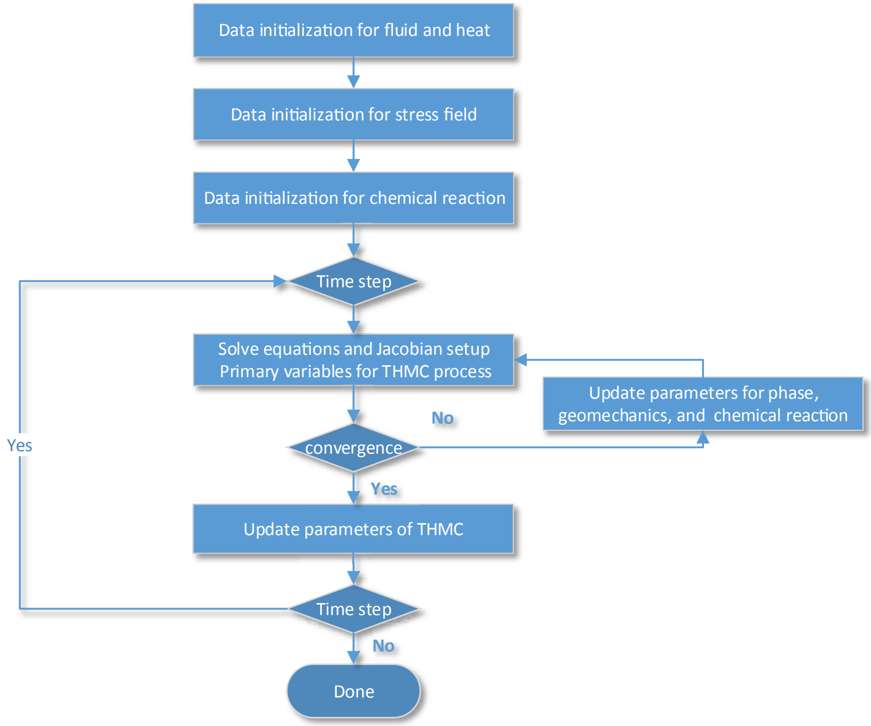

Fig. 4. The flow chart of the proposed fully coupled THMC simulator.

Table 1
Initial parameters for the THMC Model.

Hydrological parameter	
Permeability	10^{-13} m^2
Formation thickness	100 m
Formation length	10000 m
Porosity	0.30
Temperature	75° C
Initial pressure	2×10^7 Pa
CO_2 injection rate	90 kg/s
CO_2 enthalpy	5.632×10^5 J/kg
Relative permeability	
Liquid	Van Genuchten Function (1980)
Gas	Corey Function (1954)
Capillary pressure	Van Genuchten function (1980)
Stress	
Biot coefficient	1.0
Poisson's ratio	0.25
Young's modulus	5.0×10^9 Pa
Initial mean stress	4.71×10^7 Pa
Linear thermal expansion	1×10^{-5} 1/° C
Chemical Species Concentration	
H^+	0.4320×10^{-8} mol/l
HCO_3^-	0.1960×10^{-7} mol/l
Ca^{2+}	0.4737×10^{-5} mol/l
SiO_2(aq)	0.8603×10^{-10} mol/l
AlO_2^-	0.1078×10^{-11} mol/l
Kinetic Reaction Rate Constant	
Anorthite	2.5119×10^{-12} mol/m^2/s
Kaolinite	6.9183×10^{-14} mol/m^2/s

that only small amounts of the primary chemical species in the original aquifer water. In terms of geochemical reaction, 3 runs have been designed to evaluate the effects of pure CO_2 dissolution, mineral dissolution under equilibrium condition and mineral dissolution/precipitation under kinetic condition, each run of the model has different mineral compositions. Each run of the model has two scenarios: isothermal and non-isothermal, in order to exam the thermal effect on the THMC processes. The pressure and stress changes dramatically during CO_2 injection period, therefore we analyze the thermal, hydrological, and geomechanical effects in this section.

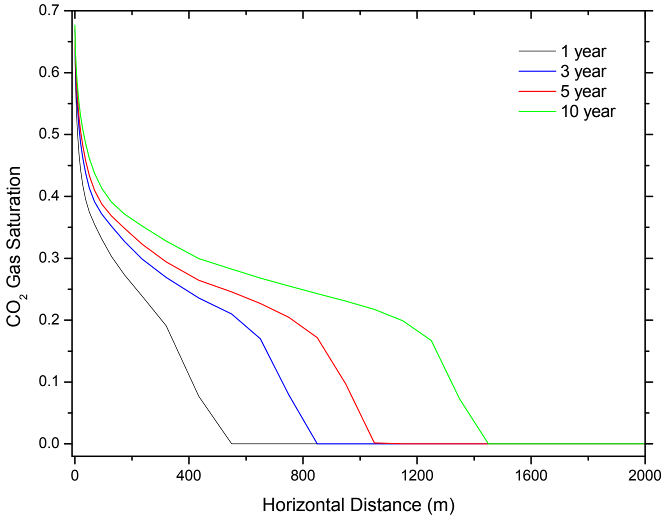

Fig. 6. CO_2 gas saturation evolution subjected to low temperature supercritical CO_2 injection.

3.1.1. The hydrological and thermal effects of low temperature supercritical CO_2 injection

For the numerical solution, two scenarios for this THMC model is conducted: the first one under non-isothermal condition, and the second one is isothermal condition. Fig. 5 shows the spatial distribution of pressure profile for non-isothermal case. Fig. 6 shows the spatial distribution of CO_2 gas saturation profile for non-isothermal cases. The profiles for pressure and gas saturation after 1 year, 3 years, 5 years and 10 years are much similar for both cases. The thermal effect do not have a significant impact on the pressure and fluid transport subject to CO_2 injection.

In Fig. 5, the pressure continues to build up in the two phase mixtures areas, and then moves laterally with CO_2 injecting into saline aquifer. The pressure near the injection point continues to increase after 1 year, then tends to decrease with the pressure

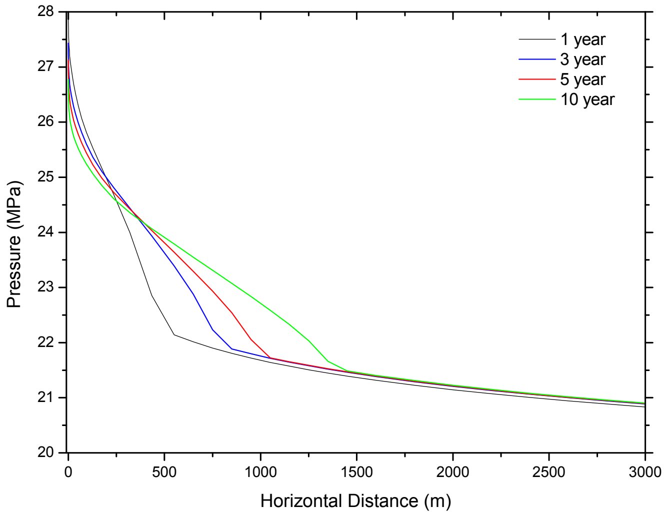

Fig. 5. Pressure evolution subjected to low temperature supercritical CO_2 injection.

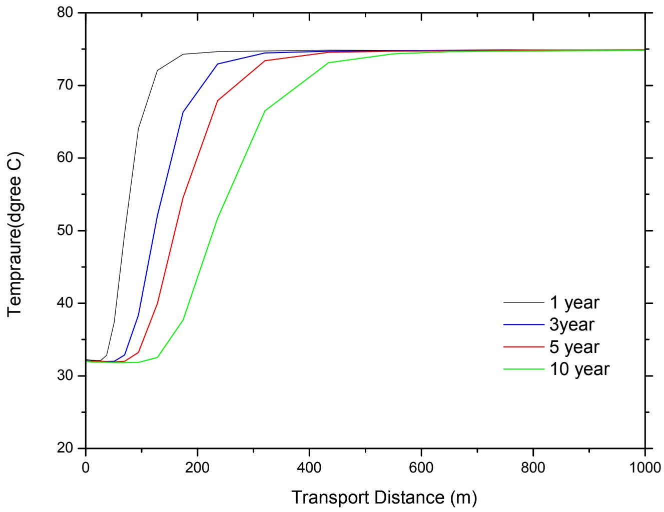

Fig. 7. Temperature evolution subjected to low temperature supercritical CO_2 injection.

transporting to far area of the aquifer, and CO_2 gas moving along the radial coordinates after 3 years, 5 years and 10 years. The pressure profiles in the two phase area have a sharp tendency compared with the single phase gas and water areas. Fig. 6 indicates the CO_2 gas front during 10 years' CO_2 injection. The CO_2 gas transports to the location of 550 m after 1 year, 850 m after 3 years, 1150 m after 5 years, and 1450 m after 10 years. The two phase of gas and liquid coexists within these distances for the different periods, and the pressure buildup is significant in the two phase area in Fig. 5.

Fig. 7 show the spatial distribution of temperature for the non-isothermal case. The gaseous CO_2 with a temperature of 32° C is injected into the formation. The temperature transports with the CO_2 gas moving laterally. The thermal effect has a significant impact on the temperature of the model. The temperature of formation become 32° C within 38 m of the wellbore after 1 year, 70 m after 3 years, 95 m after 5 years and 130 m after 10 years.

3.1.2. The thermal effect on mean stress

Figs. 8 and 9 show the spatial distribution of mean stress profile for both non-isothermal and isothermal cases. For the change in geo-mechanical field, the mean stress is proportional to the pore pressure in saline aquifer. Fig. 8 indicates that the thermal effect has a significant impact on the mean stress profile. When subjected to low temperature supercritical CO_2, the mean stress tends to decrease. Mean stress decreases significantly with a maximum value of 2×10^6 Pa in the low temperature area in Fig. 7. After that, the temperature within the area near wellbore is the same with the supercritical CO_2, the mean stress tends to increase in these areas because of the continued CO_2 injection. However, the mean stress tends to decrease when cold CO_2 transports into the far areas, then to increase after the temperatures in these areas are the same with supercritical CO_2. Fig. 9 shows that the mean stress profile has the same tendency with pressure profile during 10 years' CO_2 injection in isothermal case. The mean stress continues to build up within the area of two-phase mixtures. The mean stress increases rapidly when the front of two phase area moves laterally with CO_2 injection. Figs. 10 and 11 show the spatial distribution of volumetric strain profile for both non-isothermal and isothermal cases. The volumetric strain is related to the surface uplift of the formation in terms of the volume change of aquifer due to CO_2 injection. The tendencies of the volumetric strain profile for both cases are the

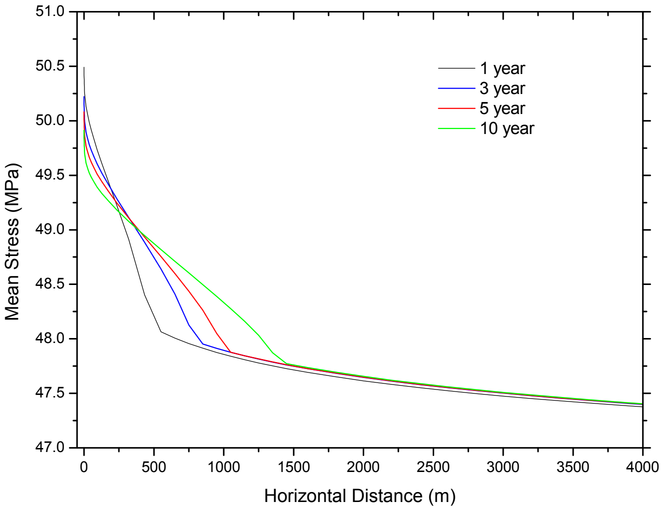

Fig. 9. Mean stress evolution subjected to supercritical CO_2 injection.

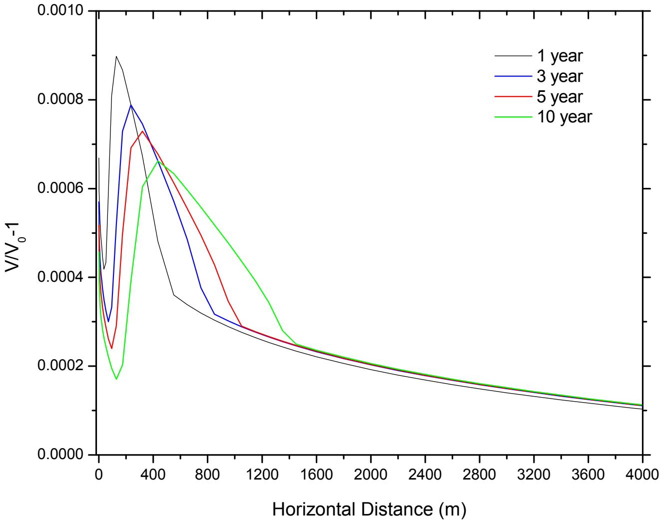

Fig. 10. Volumetric strain evolution subjected to low temperature supercritical CO_2 injection.

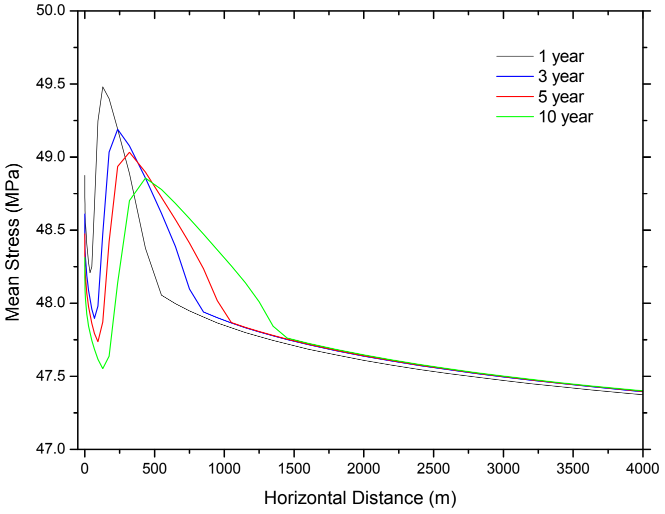

Fig. 8. Mean stress evolution subjected to low temperature supercritical CO_2 injection.

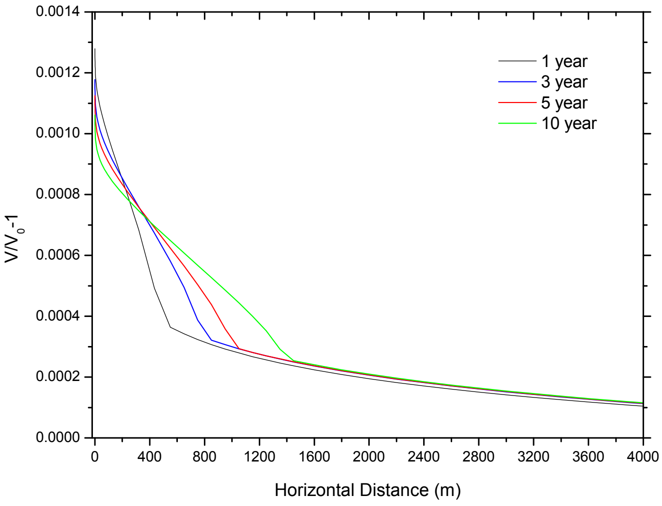

Fig. 11. Volumetric strain evolution subjected to supercritical CO_2 injection.

Table 2
Chemical reaction formulation (Wolery, 1992).

1	2	3	Aqueous complexation under equilibrium state
			$OH^- \rightarrow H_2O - H^+$
			$CO_3^{2-} \rightarrow HCO_3^- - H^+$
			$CO_2(aq) \rightarrow HCO_3^- + H^+ - H_2O$
			Gas dissolution under equilibrium state
			$CO_2(g) \rightarrow HCO_3^- + H^+ - H_2O$
			Aqueous complexation under equilibrium state
			$CaCO_3(aq) \rightarrow Ca^{2+} - H^+ + HCO_3^-$
			$CaHCO_3^+ \rightarrow Ca^{2+} + HCO_3^-$
			$CaOH^+ \rightarrow Ca^{2+} + H_2O - H^+$
			Calcite dissolution or precipitation under equilibrium state
			$CaCO_3(s) \rightarrow Ca^{2+} - H^+ + HCO_3^-$
			Aqueous complexation under equilibrium state
			$Al^{3+} \rightarrow 4H^+ + AlO_2^- - 2H_2O$
			$HAlO_2(aq) \rightarrow H^+ + AlO_2^-$
			$AlOH^{2+} \rightarrow 3H^+ - H_2O + AlO_2^-$
			$Al(OH)_2^+ \rightarrow 2H^+ + AlO_2^-$
			$Al(OH)_3(aq) \rightarrow H^+ - H_2O + AlO_2^-$
			$H_3SiO_4^- \rightarrow SiO_2(aq) - H^+ + 2H_2O$
			Kaolinite dissolution or precipitation under kinetic state
			$Al_2Si_2O_5(OH)_4 \leftrightarrow 2H^+ + 2SiO_2(aq) + H_2O + 2AlO_2^-$
			Anorthite dissolution or precipitation under kinetic state
			$Ca(Al_2Si_2O_8) \leftrightarrow Ca^{2+} + 2SiO_2(aq) + 2AlO_2^-$

same with the mean stress for both cases.

3.2. Run 1 with pure CO_2 dissolution under equilibrium

The objective of this run is to exam the effects of pure CO_2 dissolution on the THMC processes of CO_2 sequestration. The chemical reaction system is defined as pure CO_2 dissolution. The chemical reaction is only between gaseous CO_2 and H_2 O. The chemical formulations in this system are listed in Table 2. There are three primary chemical species (H_2O, H^+, and HCO_3^-) that can represent the total mass or mole in the chemical reaction system of gaseous CO_2 dissolution, in which there are three aqueous equilibrium reactions and one gas dissolution into aqueous phase. The three aqueous chemical complexations are controlled by equilibrium constant, and the CO_2 gas dissolution is controlled by partial pressure and fugacity coefficient.

Three primary aqueous species (H_2O, H^+, and HCO_3^-) and one primary gaseous species ($CO_2(g)$) have been selected to dominate this chemical reaction system ($CO_2(g)$ dissolution), there are five governing equations, of which four mass balance equations for all the primary chemical species, and one saturation index equation to solve dissolution concentration of CO_2 gas. In addition, one energy balance equation is to solve temperature, and one momentum balance equation to solve mean stress. Therefore, the equation system includes seven main equations which can represent the THMC system (CO_2 dissolution) numerically. Seven unknown variables are selected as the primary variable for the fully coupled reactive solute transport model.

3.2.1. The thermal effect on CO_2 dissolution under chemical equilibrium

Figs. 12 and 13 show the spatial distribution of dissolved concentration of $CO_2(g)$ for both non-isothermal and isothermal cases. The CO_2 dissolution only occurs within the two phase area of CO_2 and H_2O coexisting. The maximum dissolved concentrations of $CO_2(g)$ occur near the wellbore area with values of 2.32 mol/l for nonisothermal case (Fig. 12) and 1.75 mol/l for nonisothermal case (Fig. 13). It is obvious that the dissolved concentration of CO_2 gas in the lower temperature area for non-isothermal case are bigger than that for isothermal case. Therefore, thermal effect has a significant impact on the chemical reaction process. Low temperature can help more supercritical CO_2 dissolving into the aqueous phase, which can assist the solubility trapping of supercritical CO_2.

3.2.2. The geochemical effects of CO_2 dissolution under chemical equilibrium

Figs. 14–19 show the spatial distribution of the concentration of related chemical species for both non-isothermal and isothermal cases. In terms of the tendency of the profile, the independent concentration of $CO_2(aq)$ (Fig. 14), HCO_3^- (Fig. 16) and H^+ (Fig. 18) has the maximum values within the low temperature area for nonisothermal case. All these chemical species are byproducts of CO_2 dissolution. In terms of the amount of the concentration, the chemical species $CO_2(aq)$ has the biggest concentration among these three chemical species.

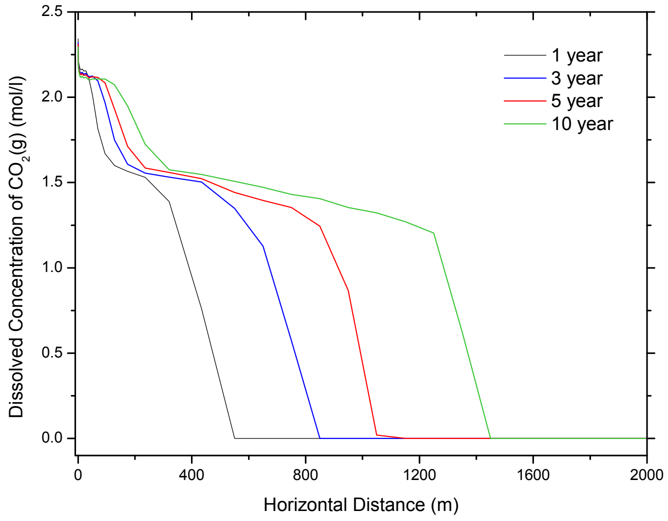

Fig. 12. Dissolved concentration of $CO_2(g)$ in aqueous phase for nonisothermal case.

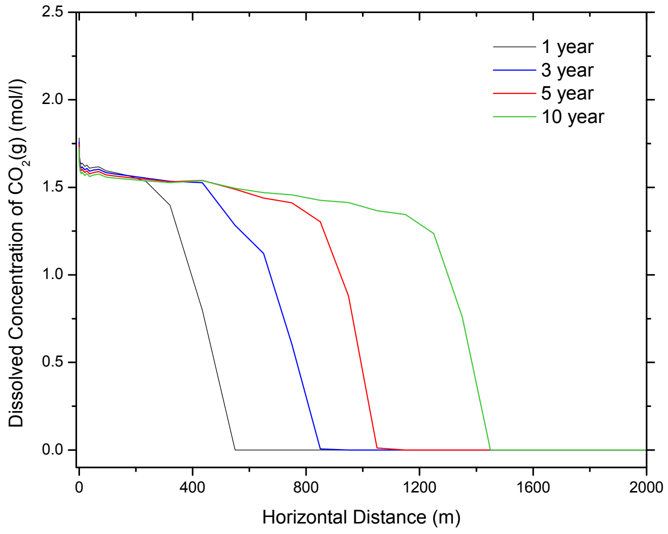

Fig. 13. Dissolved concentration of $CO_2(g)$ in aqueous phase for isothermal case.

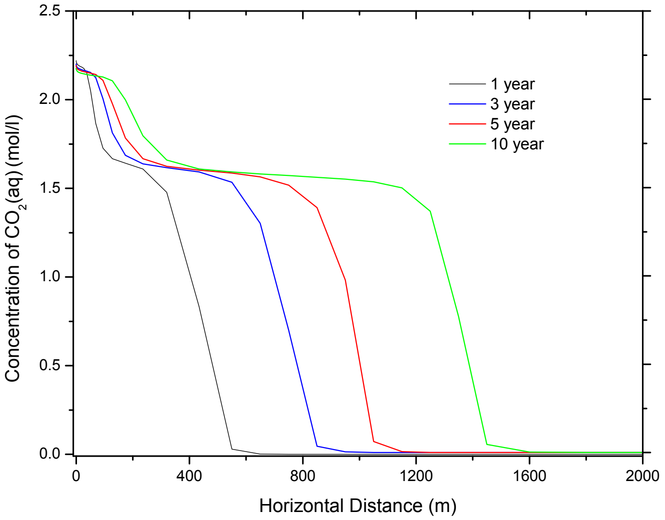

Fig. 14. Concentration of aqueous $CO_2(aq)$ subjected to low temperature supercritical CO_2 injection.

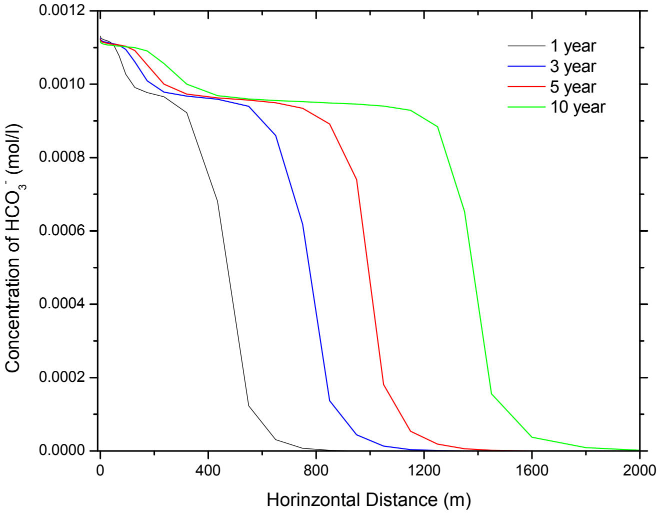

Fig. 16. Concentration of bicarbonate ion (HCO_3^-) subjected to low temperature supercritical CO_2 injection.

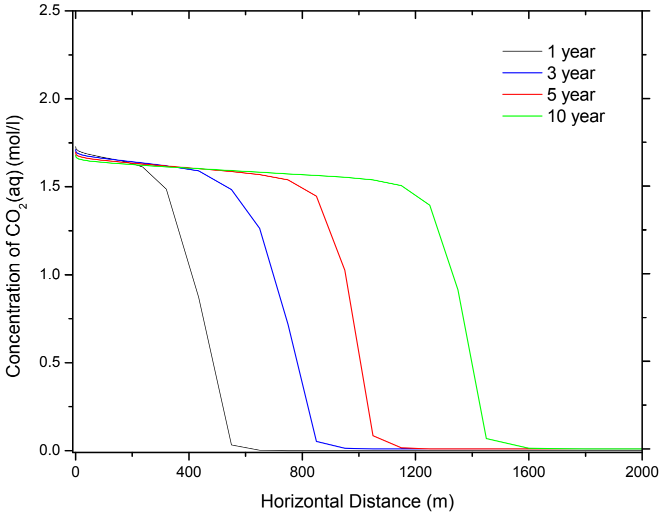

Fig. 15. Concentration of aqueous $CO_2(aq)$ subjected to supercritical CO_2 injection.

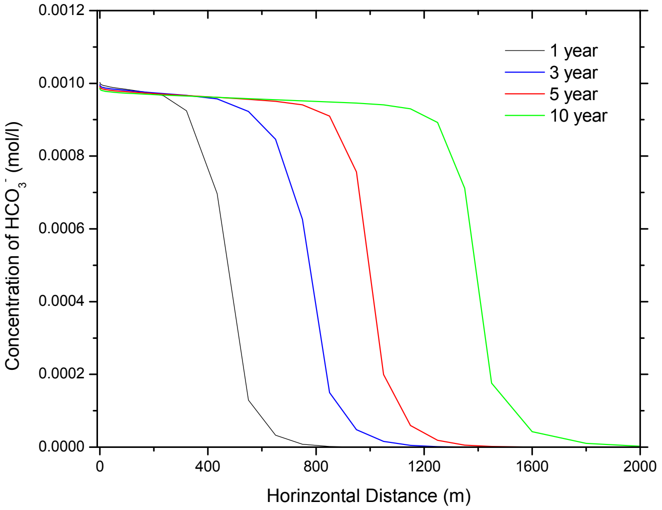

Fig. 17. Concentration of bicarbonate ion (HCO_3^-) subjected to supercritical CO_2 injection.

3.2.3. The thermal effect on pH values of CO_2 dissolution

Figs. 20–21 show the spatial distribution of the pH value for both cases. The formation is acidized in two phase area. The pH value decreases to 3.0 within the low temperature area for non-isothermal case. However, the pH value decreases to about 3.1 within the two phase area for isothermal case (Fig. 20). The dissolved concentrations of CO_2 gas in the nonisothermal case are bigger than those in isothermal case, which are shown in Figs. 12 and 13. The CO_2 dissolution releases H^+, which determines pH value. Therefore, the nonisothermal case is much more acidized.

3.3. Run 2 with mineral dissolution under equilibrium

The objective of this run is to exam the effects of CO_2 gas dissolution and mineral dissolution under equilibrium condition on the THMC processes of CO_2 sequestration. This chemical reaction system includes not only CO_2 gas dissolution but also mineral dissolution between mineral and aquifer water. The chemical reaction system is defined as CO_2 dissolution plus $CaCO_3(s)$ dissolution. Therefore, the chemical reactions involved in this chemical reaction system are between gaseous CO_2 and H_2O, and between $CaCO_3(s)$ and H_2O. The chemical formulations in this system are listed in Table 2. There are six aqueous equilibrium reactions, one gas dissolution into aqueous phase and one mineral dissolution into aqueous phase.

For the geochemical parameters, the volume fraction of $CaCO_3(s)$ in the rock is 5 percent and the $CaCO_3(s)$ dissolution is set to be in equilibrium. The other 95 percent is treated as unreactive minerals. This numerical model is to evaluate the effects of supercritical CO_2 injection on hydrological, mechanical properties, and the effect of gas and mineral dissolution on hydrological, mechanical and chemical properties, the effect of temperature on the hydrological, mechanical and chemical properties.

The geochemical system in this run is an equilibrium system ($H_2O(l)$-$CO_2(g)$-$CaCO_3(s)$), including the equilibrium geochemical

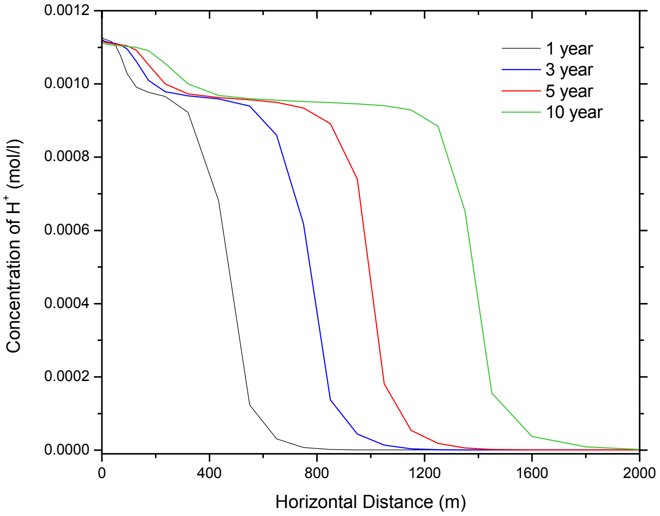

Fig. 18. Concentration of H^+ subjected to low temperature supercritical CO_2 injection.

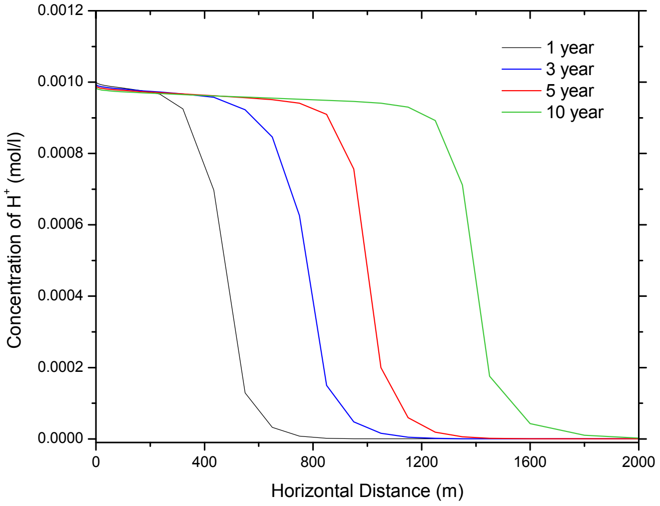

Fig. 19. Concentration of H^+ subjected to supercritical CO_2 injection.

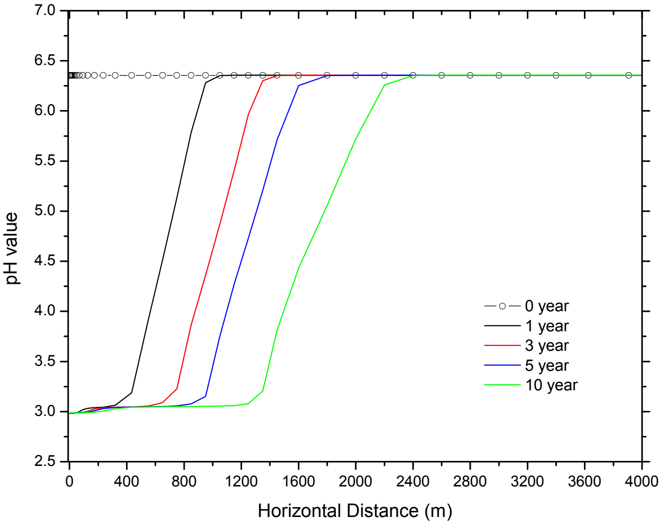

Fig. 20. pH value evolution subjected to low temperature supercritical CO_2 injection.

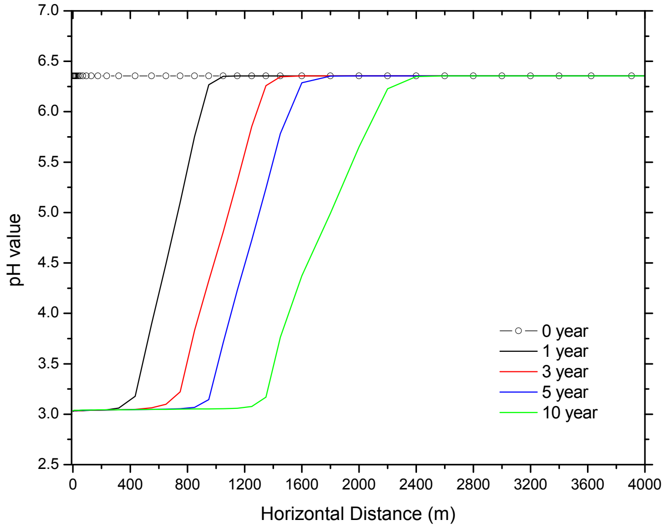

Fig. 21. pH value evolution subjected to supercritical CO_2 injection.

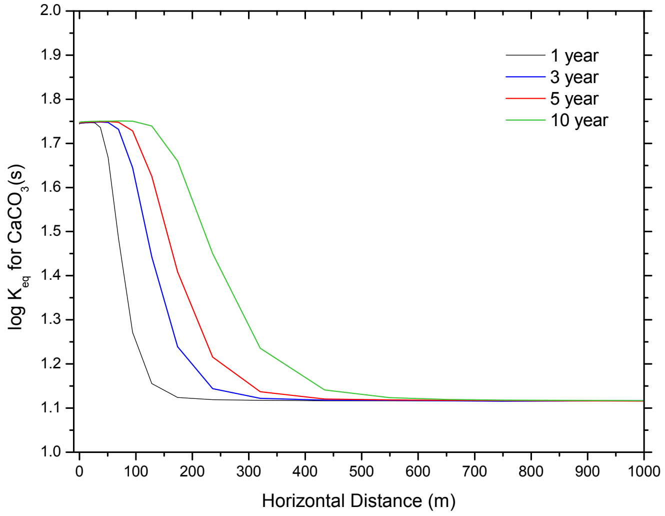

Fig. 22. Equilibrium constant of calcite ($CaCO_3$) subjected to low temperature supercritical CO_2 injection.

reactions among three phases. The four primary aqueous species (H_2O, H^+, HCO_3^-, and Ca^{2+}), one primary gaseous species ($CO_2(g)$) and one primary mineral species ($CaCO_3(s)$) are selected to represent this chemical reaction system, there are seven governing equations, of which five mass balance equation for all the primary chemical species, one gas saturation index equation to solve dissolution concentration of CO_2 gas, and one mineral saturation index equation to solve dissolution concentration of $CaCO_3(s)$. In addition, one energy balance equation is to solve temperature, and one momentum balance equation to solve mean stress. Therefore, the equation system includes nine main equations which can represent the THMC system (CO_2 dissolution + $CaCO_3(s)$ dissolution) numerically.

3.3.1. The thermal effect on the equilibrium constant of $CaCO_3$ dissolution

Fig. 22 shows the spatial distribution of equilibrium constant for

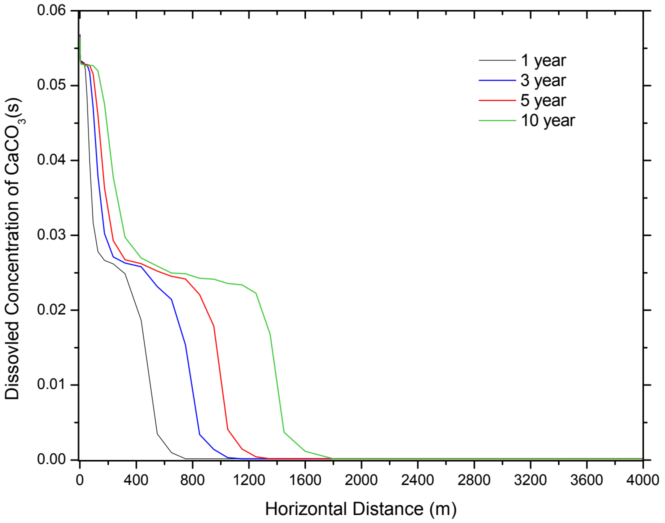

Fig. 23. Concentration of dissolved $CaCO_3(s)$ subjected to low temperature supercritical CO_2 injection.

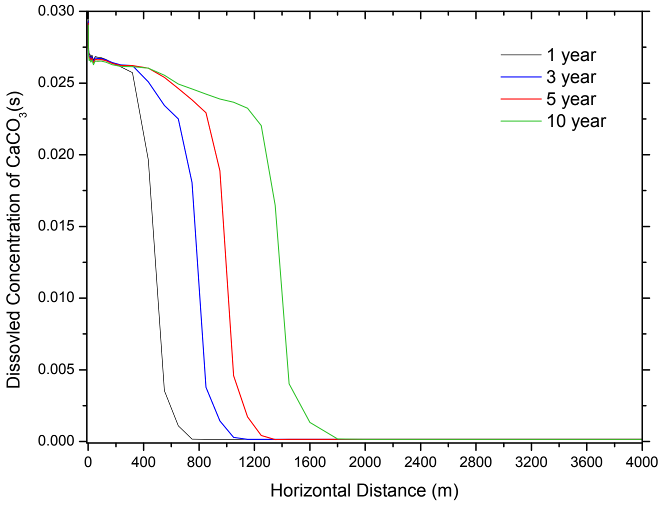

Fig. 24. Concentration of dissolved $CaCO_3(s)$ subjected to supercritical CO_2 injection.

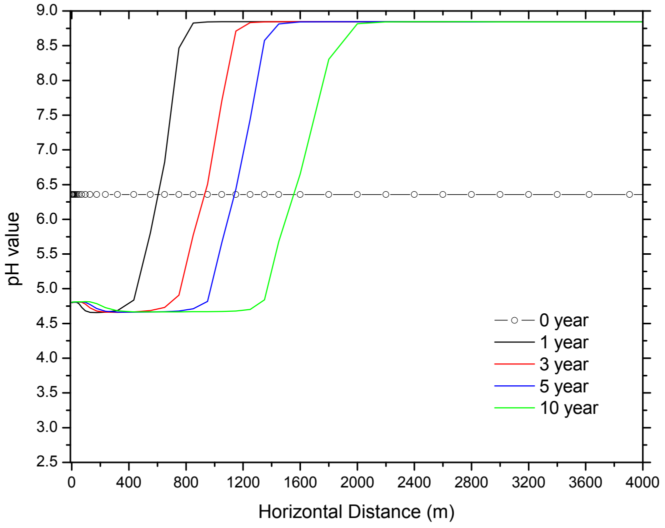

Fig. 25. pH value evolution subjected to low temperature supercritical CO_2 injection.

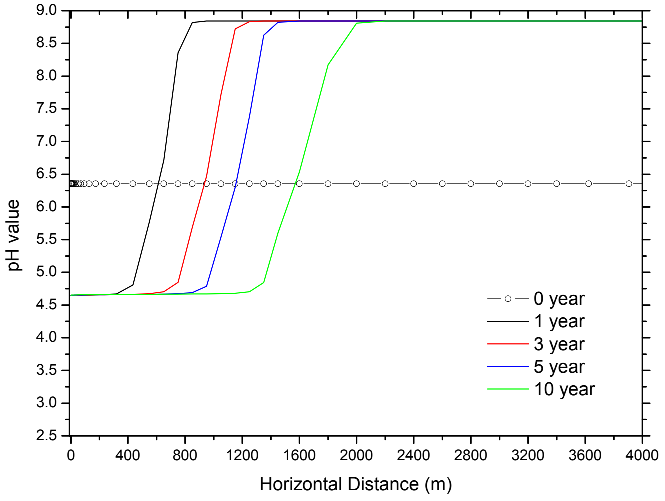

Fig. 26. pH value evolution subjected to supercritical CO_2 injection.

$CaCO_3$ dissolution for non-isothermal case. The equilibrium constant is a function of temperature. In the low temperature area, the value of log K_{eq} increases to maximum value of 1.75. However, the value of log K_{eq} maintains 1.12 at the area with original temperature. The change of equilibrium constant for $CaCO_3$ results in different chemistry in the aqueous phase compared with the isothermal case, especially for the dissolved concentration of $CaCO_3(s)$.

3.3.2. The thermal effect on $CaCO_3$ dissolution under chemical equilibrium

Figs. 23 and 24 show the spatial distribution of dissolved concentration of $CaCO_3(s)$ for both non-isothermal and isothermal cases. The $CaCO_3(s)$ dissolution only occurs within the two phase area of CO_2 and H_2O coexisting. The maximum dissolved concentrations of $CaCO_3(s)$ occur near the wellbore area with values of 0.056 mol/l for nonisothermal case (Fig. 23) and 0.026 mol/l for nonisothermal case (Fig. 24). The maximum dissolved concentration for the nonisothermal case is more than two times of isothermal case. It is indicated that there are areas with high dissolution concentrations of $CaCO_3(s)$ in Fig. 23. These areas are under low temperature condition. Therefore, the low temperature is favorable for both supercritical CO_2 dissolution and $CaCO_3(s)$ dissolution into the aqueous phase.

3.3.3. The thermal effect on pH values of $CaCO_3$ dissolution

Figs. 25–26 show the spatial distribution of the pH value for both non-isothermal and isothermal cases. The formation is acidized within the two phase area. The pH value decreases to about 4.81 within the low temperature area for nonisothermal case (Fig. 25), and the pH value decreases to about 4.65 within the two phase area for isothermal case (Fig. 26). The isothermal case is more acidized than nonisothermal case. Furthermore, the pH value in both cases is much higher than those in Section 3.2.3. The cases in Section 3.2.3 are more acidized. In this case, the $CaCO_3(s)$ dissolution is taken into account to evaluate the mutual effect of $CO_2(g)$ and $CaCO_3(s)$ dissolutions on the chemistry. The CO_2 dissolution

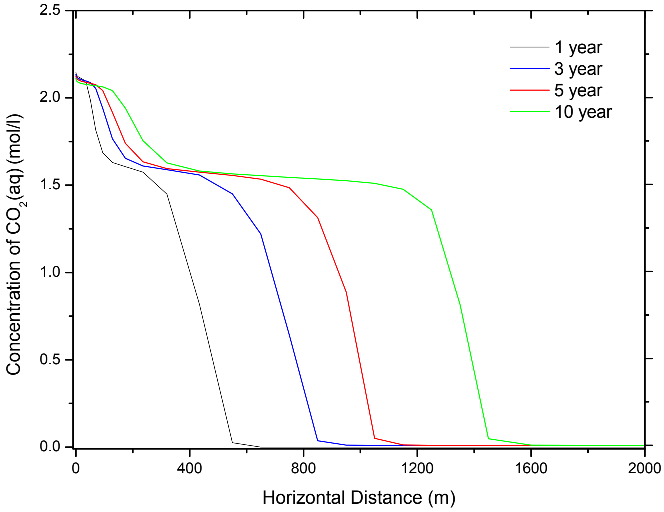

Fig. 27. Concentration of aqueous $CO_2(aq)$ subjected to low temperature supercritical CO_2 injection.

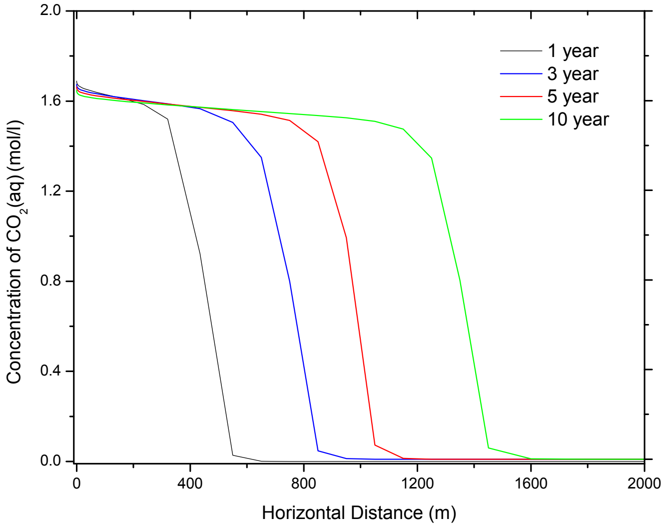

Fig. 28. Concentration of aqueous $CO_2(aq)$ subjected to supercritical CO_2 injection.

releases large amount of H^+, which is consumed by the dissolution of $CaCO_3(s)$. Therefore, the case in this section is less acidized. Moreover, the pH values within the areas close to wellbore in nonisothermal case are higher than those in isothermal case in Fig. 25, especially within 38 m of the wellbore after 1 year, 70 m after 3years, 95 m after 5 years and 130 m after 10 years. Low temperature areas have larger dissolved concentrations of $CaCO_3(s)$. More chemical species H^+ is consumed in these areas for nonisothermal case. Therefore, pH value is higher in these areas in the nonisothermal case.

3.3.4. *The geochemical effects of CO_2 dissolution and $CaCO_3$ dissolution*

Figs. 27–30 show the spatial distribution of the concentration of associate chemical species for both $CO_2(g)$ and $CaCO_3(s)$ dissolutions in non-isothermal and isothermal cases. $CO_2(aq)$ and HCO_3^- are the byproducts of $CO_2(g)$ dissolution. Figs. 27 and 28 show the spatial distribution of concentration of $CO_2(aq)$ for both cases. The maximum concentrations of $CO_2(aq)$ are 2.15 mol/l for nonisothermal case and 1.69 mol/l for isothermal case. The magnitudes of these values are similar with those in Figs. 14 and 15 of Section 3.2.3. It is indicated that the $CaCO_3(s)$ dissolution does not have a significant impact on the concentration of $CO_2(aq)$ for $CO_2(g)$ dissolution. Furthermore, Figs. 29 and 30 show the spatial distribution of concentration of HCO_3^- for both cases. The maximum concentrations of HCO_3^- are 0.095 mol/l for nonisothermal case and 0.050 mol/l for isothermal case. In the low temperature area, the concentrations of HCO_3^- are higher than those in isothermal case. However, the magnitudes of these values are much bigger than those in Figs. 16 and 17 of run 1. The maximum concentrations of HCO_3^- are 0.0015 mol/l for nonisothermal case (Fig. 16) and 0.0010 mol/l for isothermal case (Fig. 17). The values in these cases are about six times of those in Section 3.2.3. The concentration of HCO_3^- comes from both $CO_2(g)$ and $CaCO_3(s)$ dissolutions. It is obvious that majority of the HCO_3^- is released by $CaCO_3(s)$ dissolutions.

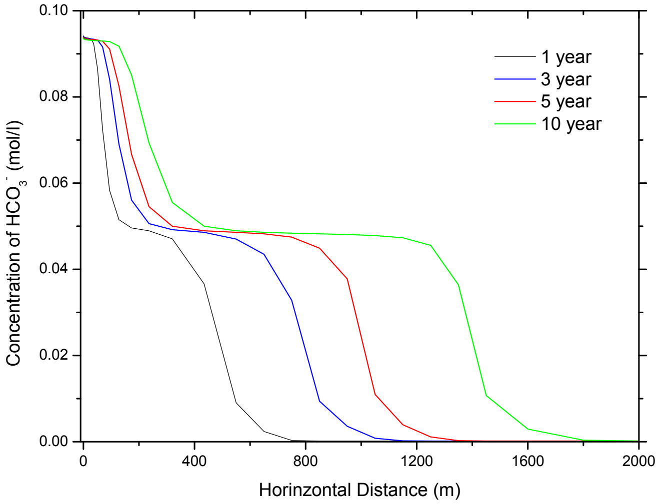

Fig. 29. Concentration of bicarbonate ion (HCO_3^-) subjected to low temperature supercritical CO_2 injection.

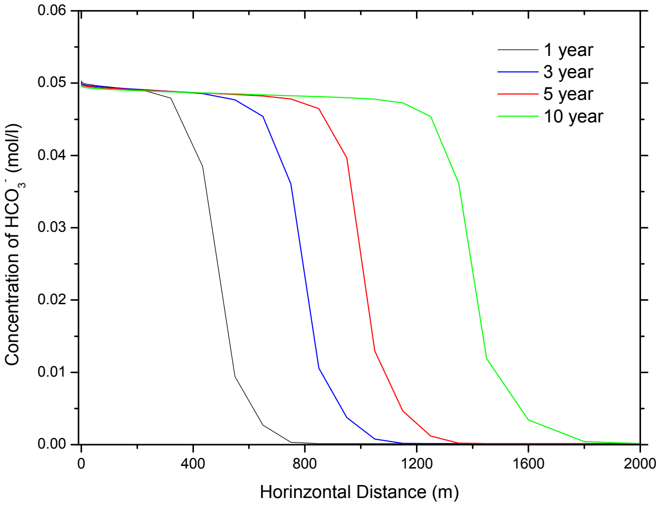

Fig. 30. Concentration of bicarbonate ion (HCO_3^-) subjected to supercritical CO_2 injection.

3.4. Run 3 with mineral dissolution and precipitation under kinetics

The objective of this run is to evaluate the effects of CO_2 gas dissolution and kinetic reactions on the THMC processes of CO_2 geo-sequestration. In this case, the chemical reaction system includes the dissolution and precipitation of multiple minerals (calcite, kaolinite and anorthite). This chemical reactions are not only equilibrium dissolutions of gas and mineral but also kinetic dissolutions and precipitations of minerals. All the chemical reaction are between gaseous CO_2 and water, and between solid mineral and water. The example problems of CMG GEM-GHG module also has selected calcite, kaolinite and anorthite minerals in the geochemical system. Anorthite is a typical plagioclase feldspar mineral, kaolite is a typical clay mineral, and calcite is typical carbonate mineral. These three minerals are the typical composition for the target saline aquifer.

The initial concentrations of the primary chemical species in this model is given in Table 1. For the geochemical parameters, the initial volume fraction of $CaCO_3(s)$ in the rock is 5.88 percent and the $CaCO_3(s)$ dissolution/precipitation is set to be in equilibrium. The initial volume fractions of kaolinite and anorthite in the rock are 5.76 percent and 5.88 percent. The dissolution/precipitation of kaolinite and anorthite are set to be in kinetic condition. The other 82.48 percent is treated as unreactive minerals. The supercritical CO_2 is injected for 10 yeas and sequestrated for 800 years. This THMC model is to evaluate the thermal effects on the long term CO_2 sequestration, the effects of kinetic reaction on the dissolution of supercritical CO_2.

The chemical formulations in this geochemical system are listed in Table 2. There are six primary chemical species (H_2O, H^+, HCO_3^-, Ca^{2+}, SiO_2 and AlO_2^-) that can represent the total mass or mole in the chemical reaction system of gaseous CO_2 dissolution and mineral dissolution/precipitation, in which there are twelve aqueous equilibrium reactions, one gas dissolution into aqueous phase under equilibrium condition, one mineral dissolution into aqueous phase under equilibrium condition, and two mineral dissolution or precipitation into aqueous phase under kinetic condition. All of the potential chemical reactions occurring in aqueous phase are set to be equilibrium. The kaolinite and anorthite dissolution/precipitation and dissolution/precipitation are controlled by kinetic reaction rate.

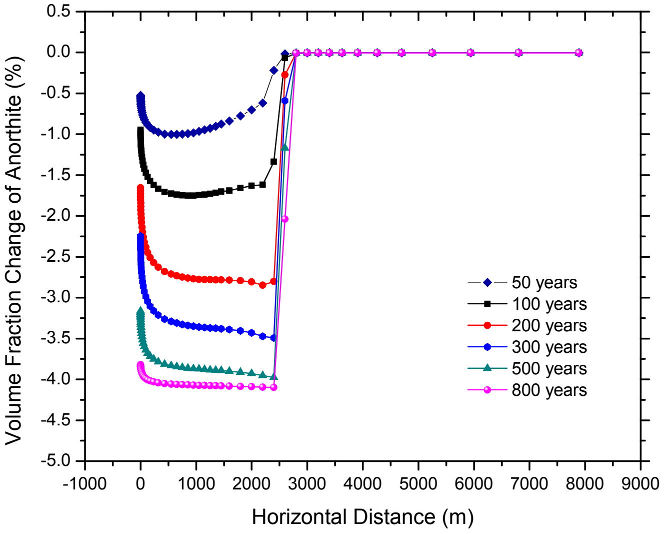

Fig. 32. Volume fraction change of anorthite subjected to supercritical CO_2 injection.

The six primary aqueous species (H_2O, H^+, HCO_3^-, Ca^{2+}, SiO_2 and AlO_2^-), one primary gaseous species ($CO_2(g)$) and three primary mineral species ($CaCO_3(s)$, $Al_2Si_2O_5(OH)_4(s)$, and $Ca(Al_2Si_2O_8)(s)$) are selected to represent this chemical reaction system, there are nine governing equations, of which seven mass balance equations for all the primary chemical species, one gas saturation index equation to solve dissolution concentration of CO_2 gas, and one mineral saturation index equation to solve dissolution concentration of $CaCO_3(s)$. In addition, one energy balance equation is to solve temperature, and one momentum balance equation to solve mean stress. The equation system includes eleven main equations which can represent the THMC system (CO_2 dissolution + calcite dissolution + kaolinite dissolution/precipitation + anorthite dissolution/precipitation) numerically. This THMC model in run 3 has the most complex geochemical reaction system. Therefore, the

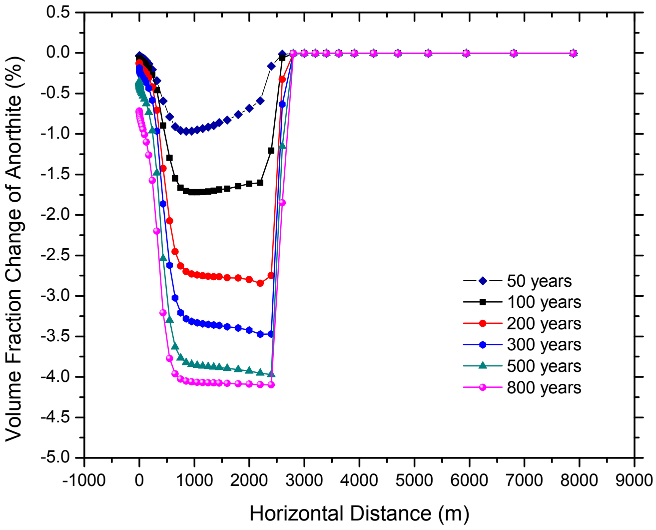

Fig. 31. Volume fraction change of anorthite subjected to low temperature supercritical CO_2 injection.

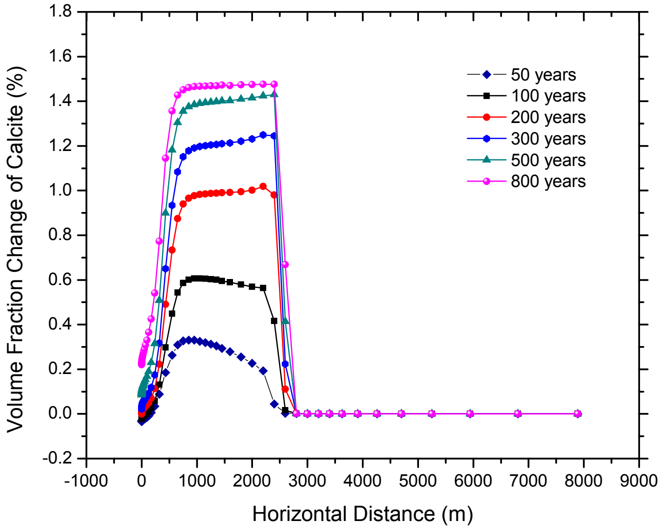

Fig. 33. Volume fraction change of calcite subjected to low temperature supercritical CO_2 injection.

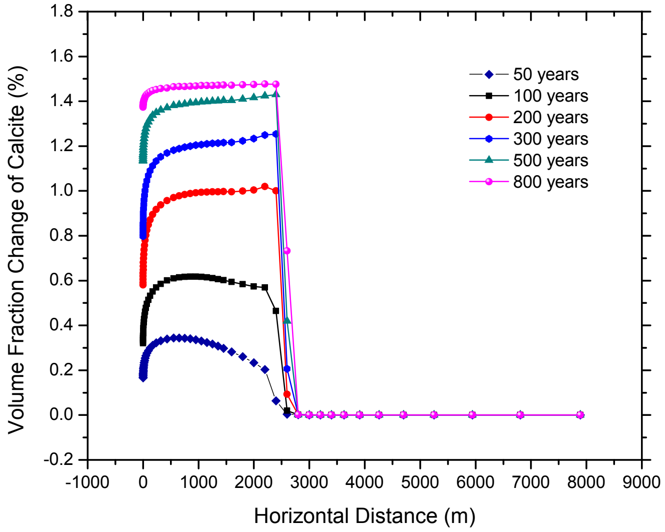

Fig. 34. Volume fraction change of calcite subjected to supercritical CO_2 injection.

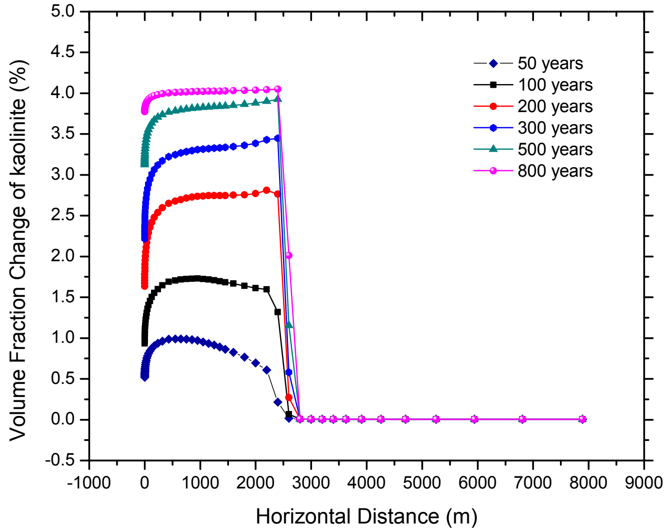

Fig. 36. Volume fraction change of kaolinite subjected to supercritical CO_2 injection.

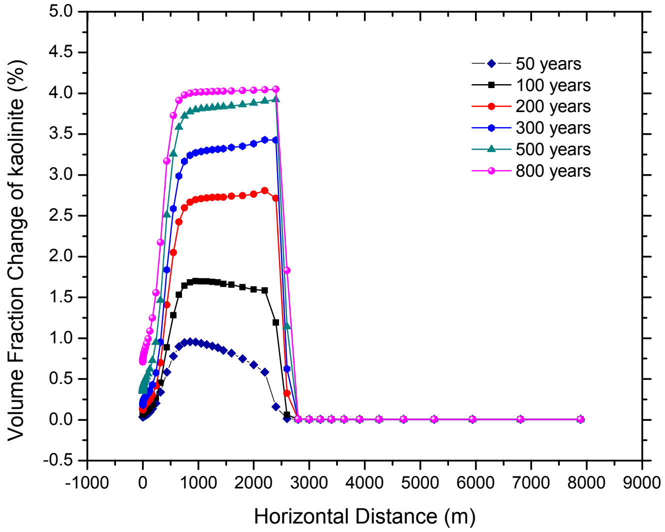

Fig. 35. Volume fraction change of kaolinite subjected to low temperature supercritical CO_2 injection.

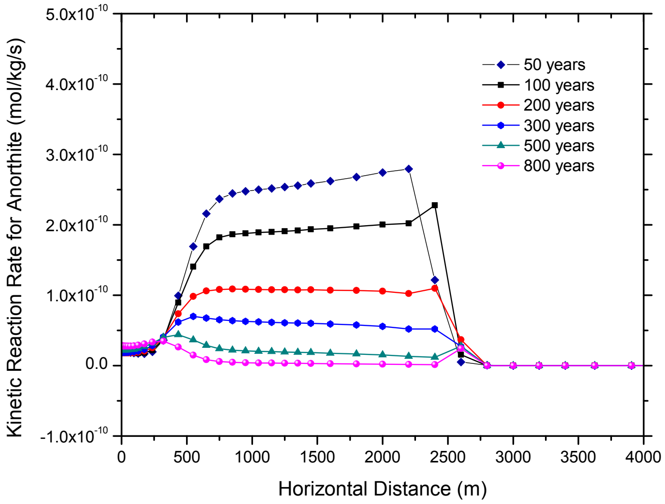

Fig. 37. Kinetic reaction rate of anorthite subjected to low temperature supercritical CO_2 injection.

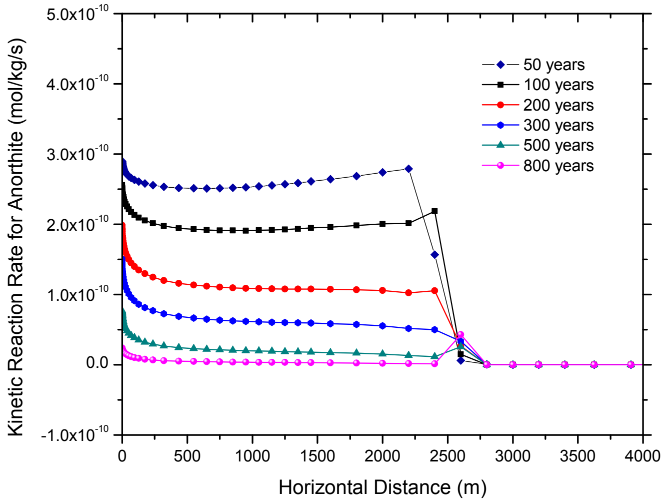

Fig. 38. Kinetic reaction rate of anorthite subjected to supercritical CO_2 injection.

detailed derivation of this THMC model can provide a good example to show the numerical equation system in Appendix A.

3.4.1. The thermal effect on kinetic reaction rate of anorthite dissolution

Figs. 37 and 38 show the kinetic reaction rate profile of anorthite dissolution during 800 years' storage period for both cases. Positive value of kinetic reaction rate represents dissolution and negative value represents precipitation. It is indicated that the kinetic reaction rate for anorthite dissolution reaches the maximum value of about 3.0×10^{-10} mol/kg H_2O/s in the areas with high temperature, and it is around 0.2×10^{-10} mol/kg H_2O/s within about 500 m close to the wellbore areas with low temperature (Fig. 37). The kinetic reaction rate under high temperature condition of 70° C is fifteen times higher than that under low temperature condition of 30° C. Fig. 38 shows the kinetic reaction rate of anorthite dissolution for

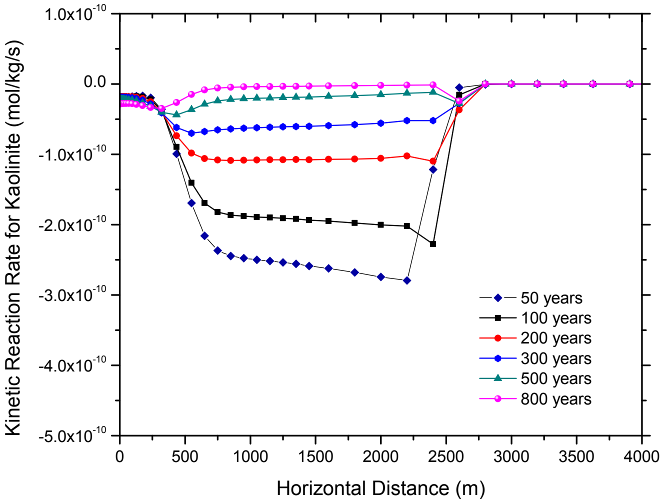

Fig. 39. Kinetic reaction rate of kaolinite subjected to low temperature supercritical CO_2 injection.

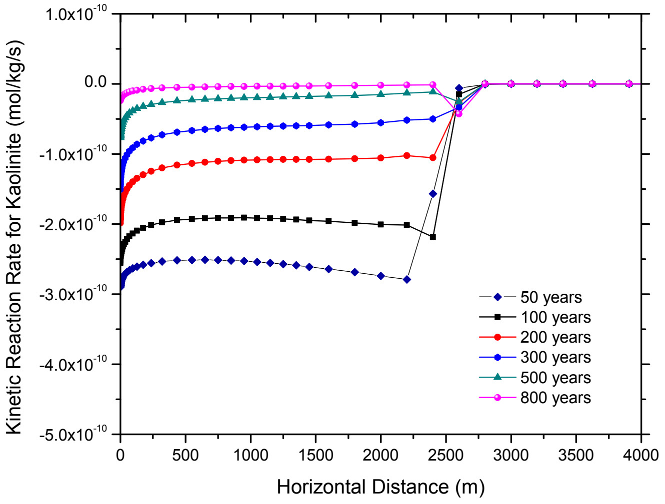

Fig. 40. Kinetic reaction rate of kaolinite subjected to supercritical CO_2 injection.

isothermal case, and its value is decreasing along the horizontal distance.

3.4.2. *The thermal effect on kinetic reaction rate of kaolinite precipitation*

Figs. 39 and 40 show the kinetic reaction rate profile of kaolinite precipitation during 800 years' storage period for both cases. It is shown in Fig. 39 that the kinetic reaction rate for kaolinite precipitation reaches the maximum value of about 3.0×10^{-10} mol/kg H_2O/s in the areas with high temperature, and it is less than 0.3×10^{-10} mol/kg H_2O/s within about 400 m close to the wellbore areas. Fig. 40 shows the kinetic reaction rate of kaolinite precipitation for isothermal case, and its value of kinetic reaction rate is decreasing along the horizontal distance.

3.4.3. *The thermal and geochemical effect on anorthite dissolution volume*

Figs. 31–36 show the volume fraction change profile for rock minerals during 800 years' storage period for both non-isothermal and isothermal cases. It is obvious that anorthite tends to dissolved to the maximum amount after 800 years, and koalinite and calcite tend to precipitate to the maximum amounts at 800 years. Figs. 31 and 32 show the volume fraction change profile of anorthite during 800 years' storage period for both cases. It is obvious that the volume fractions of anorthite dissolved into the mineral phase achieve the maximum values (about 4 percent) in the area with high temperature. However, the volume fractions of anorthite dissolved into aqueous phase is only a small amount in the areas with low temperature. The volume fraction of anorthite only decreases by 0.6 percent at the injection point (Fig. 31) after 800 years for non-isothermal case, but the volume fraction of anorthite decreases by 3.75 percent at the injection point (Fig. 32) after 800 years for the isothermal case. Fig. 32 shows that the volume fractions of anorthite precipitated into mineral phase are larger in the areas near wellbore for isothermal case.

3.4.4. *The thermal and geochemical effect on calcite precipitation volume*

Figs. 33 and 34 show the volume fraction change profile of calcite during 800 years' storage period for both cases. At the injection period, the calcite tends to dissolved into the aqueous phase, as shown in Figs. 23 and 24. It is an equilibrium chemical reaction controlled by equilibrium constant. The chemical species of Ca^{2+} and HCO_3^- is not supersaturated at the injection period due to the short time period. With time increasing, kinetic chemical reaction dominates the chemical system. These two chemical species become supersaturated after the dissolution of anorthite. It is obvious that the calcite precipitates into mineral phase in Figs. 33 and 34. It is obvious that the volume fractions of calcite precipitated into the mineral phase achieve the maximum values (about 4 percent) in the area with high temperature. However, the volume fractions of calcite precipitated into mineral phase is only a small amount (less than 2 percent) in the areas with low temperature.

3.4.5. *The thermal and geochemical effect on kaolinite precipitation volume*

Figs. 35 and 36 show the volume fraction change profile of

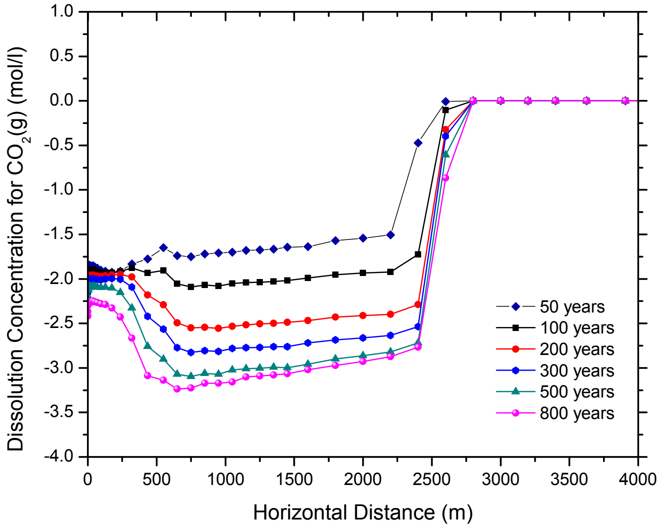

Fig. 41. Dissolution concentration of CO_2(g) subjected to low temperature supercritical CO_2 injection.

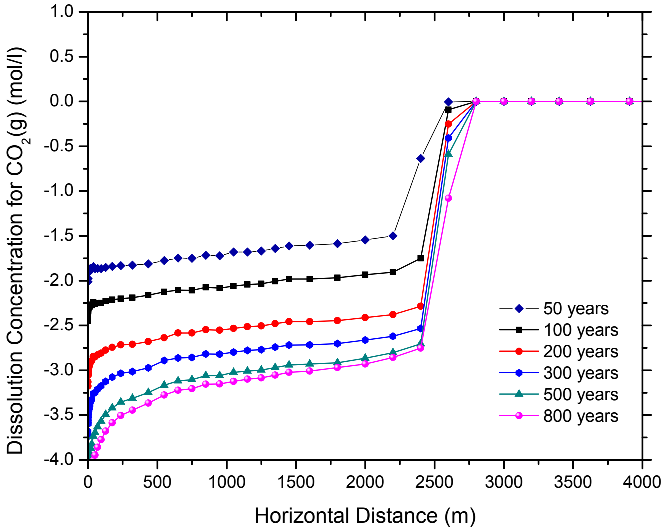

Fig. 42. Dissolution concentration of CO_2(g) subjected to supercritical CO_2 injection.

kaolinite during 800 years' storage period for both cases. The volume fractions of kaolinite precipitated into the mineral phase achieve the maximum values (about 4 percent) in the area with high temperature. However, the volume fractions of kaolinite precipitated into mineral phase is only a small amount (less than 7 percent) in the areas with low temperature. The tendencies of Figs. 35 and 36 are similar with Figs. 33 and 34. Therefore, the thermal effect has a significant effect on the evolution of rock compositions.

Figs. 32, 34 and 36 show the volume faction change profiles of anorthite, calcite and kaolinite during 800 years' storage period for isothermal case. Figs. 38 and 40 show the kinetic reaction rate profiles of anorthite and kaolinite during 800 years' storage period for isothermal case. It is indicated that the absolute value of volume fraction change for these minerals are smaller within 400 m of wellbore than the far areas. However, the kinetic reaction rates for anorthite and kaolinite tend to be larger in the wellbore area. The supercritical CO_2 is highly saturated in the wellbore areas due to large amount of supercritical CO_2 injection. The amount of water near wellbore area is less than the far areas. Therefore, there is not much rock minerals dissolved/precipitated near wellbore, even though the kinetic reaction rate is larger in the area near wellbore.

3.4.6. The thermal and geochemical effect on CO_2 dissolution concentration

Figs. 41 and 42 show the spatial distribution of dissolved concentration of CO_2(g) for both non-isothermal and isothermal cases. The CO_2 dissolution only occurs within the two phase area of CO_2 and H_2O coexisting. Fig. 41 shows that the amount of CO_2 dissolved into aqueous phase in the area with low temperature is larger than the other areas at 50 years' storage period, after that, it becomes smaller than the other areas with time increasing. The kinetic reaction starts to dominate the chemical reaction system during long term storage period, and the kinetic reaction rate tend to be larger under high temperature condition. Therefore, the supercritical CO_2 dissolved faster to supply HCO_3^- for calcite precipitation. Fig. 42 shows that the dissolved concentration of CO_2(g) is decreasing along horizontal distance.

4. Concluding marks

- A novel mathematical model of the THMC processes is developed. The fully coupled computational framework is proposed and used to simulate reactive transport of supercritical CO_2 in subsurface formation with geo-mechanics. The novel framework is designed to keep a generalized computational structure, which can be easily applied for the numerical simulation of other THMC processes. Applications of THMC transport models are presented to analyze the THMC process quantitatively, especially the coupled effects of geo–chemical reactions and geo-mechanics on CO_2 geo-sequestration, the long term fate of CO_2 and its sensitivity mineralogical compositions with respect to key minerals.
- For the coupled THMC processes during the CO_2 geo-sequestration, the geochemical reactions do not have significant impact on pore pressure, mean stress and temperature. But, the thermal energy transport affects the mean stress and geochemical reactions in the saline aquifer, especially for cold CO_2 injection into deep saline aquifer. Low temperature accelerates equilibrium dissolution of gas and mineral, but slows down kinetic dissolution/precipitation of minerals, such as anorthite and kaolinite.
- After cold supercritical CO_2 (32° C) injection into saline aquifer (75° C), the area within 600 m become low temperature zone. In the low temperature zone, the dissolved concentration of CO_2 increases by 30 percent under equilibrium condition, and the dissolved concentration of calcite increases by 100 percent under equilibrium condition. During long term CO_2 geo-sequestration, the kinetic chemical reactions dominate the chemical reaction pathway for supercritical CO_2. The kinetic reaction rates for mineral dissolution and precipitation become lower and lower with time increasing during storage period, because the geochemical reaction system reach equilibrium within long term period. The rock minerals at the interface of two phase zone and water zone react significantly and rapidly under kinetic conditions. When anorthite (a typical mineral of plagioclase group) and kaolinite (a typical mineral of clay minerals) are present in the formation, the dissolution of anorthite leads to kaolinite precipitation.

Acknowledgment

This work is supported by the U.S. Department of Energy under Contract No. DE-FE0000988, Simulation of Coupled Processes of Flow, Transport, and Storage of CO_2 in Saline Aquifers. Special thanks are due to the Energy Modeling Group (EMG) of Department of Petroleum Engineering at Colorado School of Mines and to Foundation Computer Modeling Group (CMG). Special thanks to Dr. Tianfu Xu, who is a scientist at Lawrence Berkeley National Laboratory and the developer of TOUGHREACT simulator.

Appendix A. Derivation for THMC Model with Chemical Kinetic Reactions

There are six primary chemical species (H_2O, H^+, HCO_3^-, Ca^{2+}, SiO_2 and AlO_2^-) that can represent the total mass or mole in the chemical reaction system of gaseous CO_2 dissolution and mineral dissolution/precipitation, in which there are twelve aqueous equilibrium reactions, one gas dissolution into aqueous phase under equilibrium condition, one mineral dissolution into aqueous phase under equilibrium condition, and two mineral dissolution or precipitation into aqueous phase under kinetic condition. The twelve aqueous chemical complex chemical reactions are controlled by aqueous equilibrium constant, the CO_2 gas dissolution is controlled by partial pressure and fugacity coefficient, and the calcite dissolution is controlled by equilibrium constant for mineral dissolution, the kaolinite dissolution/precipitation and the anorthite dissolution/precipitation are controlled by kinetic reaction rate. These fourteen chemical reactions can be expressed by Eqs. A.1 – A.18:

$$c_{\mathrm{OH^-}} = K_{\mathrm{OH^-}}^{-1}\gamma_{\mathrm{OH^-}}^{-1}\left[\frac{c_{\mathrm{H_2O}}\gamma_{\mathrm{H_2O}}}{c_{\mathrm{H^+}}\gamma_{\mathrm{H^+}}}\right] \tag{A.1}$$

$$K_{\mathrm{CaCO_3(s)}} = \frac{c_{\mathrm{Ca^{2+}}}\gamma_{\mathrm{Ca^{2+}}}c_{\mathrm{HCO_3^-}}\gamma_{\mathrm{HCO_3^-}}}{c_{\mathrm{H^+}}\gamma_{\mathrm{H^+}}} \tag{A.14}$$

$$r_{\mathrm{Al_2Si_2O_5(OH)_4(s)}} = \pm K_{\mathrm{Al_2Si_2O_5(OH)_4(s)}}A_{\mathrm{Al_2Si_2O_5(OH)_4(s)}}\Big|1 - \Omega_{\mathrm{Al_2Si_2O_5(OH)_4(s)}}\Big| \tag{A.15}$$

$$\Omega_{\mathrm{Al_2Si_2O_5(OH)_4(s)}} = K_{\mathrm{m}}^{-1}\left[1\right]\frac{c_{\mathrm{H^+}}^2\gamma_{\mathrm{H^+}}^2\cdot c_{\mathrm{SiO_2(aq)}}^2\gamma_{\mathrm{SiO_2(aq)}}^2\cdot c_{\mathrm{H_2O}}\gamma_{\mathrm{H_2O}}\cdot c_{\mathrm{AlO_2^-}}^2\gamma_{\mathrm{AlO_2^-}}^2}{1}\Big]1\Big] \tag{A.16}$$

$$c_{\mathrm{CO_3^{2-}}} = K_{\mathrm{CO_3^{2-}}}^{-1}\gamma_{\mathrm{CO_3^{2-}}}^{-1}\left[\frac{c_{\mathrm{HCO_3^-}}\gamma_{\mathrm{HCO_3^-}}}{c_{\mathrm{H^+}}\gamma_{\mathrm{H^+}}}\right] \tag{A.2}$$

$$c_{\mathrm{CO_2(aq)}} = K_{\mathrm{CO_2(aq)}}^{-1}\gamma_{\mathrm{CO_2(aq)}}^{-1}\left[\frac{c_{\mathrm{H^+}}\gamma_{\mathrm{H^+}}\cdot c_{\mathrm{HCO_3^-}}\gamma_{\mathrm{HCO_3^-}}}{c_{\mathrm{H_2O}}\gamma_{\mathrm{H_2O}}}\right] \tag{A.3}$$

$$c_{\mathrm{CaCO_3(aq)}} = K_{\mathrm{CaCO_3(aq)}}^{-1}\gamma_{\mathrm{CaCO_3(aq)}}^{-1}\left[\frac{c_{\mathrm{Ca^{2+}}}\gamma_{\mathrm{Ca^{2+}}}\cdot c_{\mathrm{HCO_3^-}}\gamma_{\mathrm{HCO_3^-}}}{c_{\mathrm{H^+}}\gamma_{\mathrm{H^+}}}\right] \tag{A.4}$$

$$c_{\mathrm{CaHCO_3^-}} = K_{\mathrm{CaHCO_3^-}}^{-1}\gamma_{\mathrm{CaHCO_3^-}}^{-1}\left[\frac{c_{\mathrm{HCO_3^-}}\gamma_{\mathrm{HCO_3^-}}\cdot c_{\mathrm{Ca^{2+}}}\gamma_{\mathrm{Ca^{2+}}}}{1}\right] \tag{A.5}$$

$$c_{\mathrm{CaOH^+}} = K_{\mathrm{CaOH^+}}^{-1}\gamma_{\mathrm{CaOH^+}}^{-1}\left[\frac{c_{\mathrm{Ca^{2+}}}\gamma_{\mathrm{Ca^{2+}}}\cdot c_{\mathrm{H_2O}}\gamma_{\mathrm{H_2O}}}{c_{\mathrm{H^+}}\gamma_{\mathrm{H^+}}}\right] \tag{A.6}$$

$$c_{\mathrm{Al^{3+}}} = K_{\mathrm{Al^{3+}}}^{-1}\gamma_{\mathrm{Al^{3+}}}^{-1}\left[\frac{c_{\mathrm{H^+}}^4\gamma_{\mathrm{H^+}}^4\cdot c_{\mathrm{AlO_2^-}}\gamma_{\mathrm{AlO_2^-}}}{c_{\mathrm{H_2O}}^2\gamma_{\mathrm{H_2O}}^2}\right] \tag{A.7}$$

$$c_{\mathrm{HAlO_2(aq)}} = K_{\mathrm{HAlO_2(aq)}}^{-1}\gamma_{\mathrm{HAlO_2(aq)}}^{-1}\left[\frac{c_{\mathrm{H^+}}\gamma_{\mathrm{H^+}}\cdot c_{\mathrm{AlO_2^-}}\gamma_{\mathrm{AlO_2^-}}}{1}\right] \tag{A.8}$$

$$c_{\mathrm{AlOH^{2+}}} = K_{\mathrm{AlOH^{2+}}}^{-1}\gamma_{\mathrm{AlOH^{2+}}}^{-1}\left[\frac{c_{\mathrm{H^+}}^3\gamma_{\mathrm{H^+}}^3\cdot c_{\mathrm{AlO_2^-}}\gamma_{\mathrm{AlO_2^-}}}{c_{\mathrm{H_2O}}\gamma_{\mathrm{H_2O}}}\right] \tag{A.9}$$

$$c_{\mathrm{Al(OH)_2^+}} = K_{\mathrm{Al(OH)_2^+}}^{-1}\gamma_{\mathrm{Al(OH)_2^+}}^{-1}\left[\frac{c_{\mathrm{H^+}}^2\gamma_{\mathrm{H^+}}^2\cdot c_{\mathrm{AlO_2^-}}\gamma_{\mathrm{AlO_2^-}}}{1}\right] \tag{A.10}$$

$$c_{\mathrm{Al(OH)_3(aq)}} = K_{\mathrm{Al(OH)_3(aq)}}^{-1}\gamma_{\mathrm{Al(OH)_3(aq)}}^{-1}\left[\frac{c_{\mathrm{H^+}}\gamma_{\mathrm{H^+}}\cdot c_{\mathrm{AlO_2^-}}\gamma_{\mathrm{AlO_2^-}}}{c_{\mathrm{H_2O}}\gamma_{\mathrm{H_2O}}}\right] \tag{A.11}$$

$$c_{\mathrm{H_3SiO_4^-}} = K_{\mathrm{H_3SiO_4^-}}^{-1}\gamma_{\mathrm{H_3SiO_4^-}}^{-1}\left[\frac{c_{\mathrm{H_2O}}^2\gamma_{\mathrm{H_2O}}^2\cdot c_{\mathrm{SiO_2(aq)}}\gamma_{\mathrm{SiO_2(aq)}}}{c_{\mathrm{H^+}}\gamma_{\mathrm{H^+}}}\right] \tag{A.12}$$

$$P_{\mathrm{CO_2(g)}} = K_{\mathrm{CO_2(g)}}^{-1}\Gamma_{\mathrm{CO_2(g)}}^{-1}\left[\frac{c_{\mathrm{H^+}}\gamma_{\mathrm{H^+}}c_{\mathrm{HCO_3^-}}\gamma_{\mathrm{HCO_3^-}}}{c_{\mathrm{H_2O}}\gamma_{\mathrm{H_2O}}}\right] \tag{A.13}$$

$$r_{\mathrm{Ca(Al_2Si_2O_8)(s)}} = \pm K_{\mathrm{Ca(Al_2Si_2O_8)(s)}}A_{\mathrm{Ca(Al_2Si_2O_8)}}\Big|1 - \Omega_{\mathrm{Ca(Al_2Si_2O_8)(s)}}\Big| \tag{A.17}$$

$$\Omega_{\mathrm{Ca(Al_2Si_2O_8)(s)}} = K_{\mathrm{m}}^{-1}\left[\frac{c_{\mathrm{Ca^{2+}}}\gamma_{\mathrm{Ca^{2+}}}\cdot c_{\mathrm{SiO_2(aq)}}^2\gamma_{\mathrm{SiO_2(aq)}}^2\cdot c_{\mathrm{AlO_2^-}}^2\gamma_{\mathrm{AlO_2^-}}^2}{1}\right] \tag{A.18}$$

The mass or mole of the secondary aqueous complex can be represented by the primary species, as shown in the chemical reaction equations. The total mass or mole of each primary species can represent the total compositions of the aqueous phase. The mass or mole of the twelve secondary aqueous complexes in the aqueous phase can be added to that of the four primary chemical species. The mathematical formula for the total mass or mole of each primary species can be expressed as:

$$\begin{aligned}
C_{\mathrm{H_2O}} = c_{\mathrm{H_2O}} &- K_{\mathrm{CO_2(aq)}}^{-1}\gamma_{\mathrm{CO_2(aq)}}^{-1}\left[\frac{c_{\mathrm{H^+}}\gamma_{\mathrm{H^+}}\cdot c_{\mathrm{HCO_3^-}}\gamma_{\mathrm{HCO_3^-}}}{c_{\mathrm{H_2O}}\gamma_{\mathrm{H_2O}}}\right]\\
&+ K_{\mathrm{OH^-}}^{-1}\gamma_{\mathrm{OH^-}}^{-1}\left[\frac{c_{\mathrm{H_2O}}\gamma_{\mathrm{H_2O}}}{c_{\mathrm{H^+}}\gamma_{\mathrm{H^+}}}\right]\\
&+ K_{\mathrm{CaOH^+}}^{-1}\gamma_{\mathrm{CaOH^+}}^{-1}\left[\frac{c_{\mathrm{Ca^{2+}}}\gamma_{\mathrm{Ca^{2+}}}\bullet c_{\mathrm{H_2O}}\gamma_{\mathrm{H_2O}}}{c_{\mathrm{H^+}}\gamma_{\mathrm{H^+}}}\right]\\
&- 2K_{\mathrm{Al^{3+}}}^{-1}\gamma_{\mathrm{Al^{3+}}}^{-1}\left[\frac{c_{\mathrm{H^+}}^4\gamma_{\mathrm{H^+}}^4\cdot c_{\mathrm{AlO_2^-}}\gamma_{\mathrm{AlO_2^-}}}{c_{\mathrm{H_2O}}^2\gamma_{\mathrm{H_2O}}^2}\right]\\
&- K_{\mathrm{AlOH^{2+}}}^{-1}\gamma_{\mathrm{AlOH^{2+}}}^{-1}\left[\frac{c_{\mathrm{H^+}}^3\gamma_{\mathrm{H^+}}^3\cdot c_{\mathrm{AlO_2^-}}\gamma_{\mathrm{AlO_2^-}}}{c_{\mathrm{H_2O}}\gamma_{\mathrm{H_2O}}}\right]\\
&- K_{\mathrm{Al(OH)_3(aq)}}^{-1}\gamma_{\mathrm{Al(OH)_3(aq)}}^{-1}\left[\frac{c_{\mathrm{H^+}}\gamma_{\mathrm{H^+}}\cdot c_{\mathrm{AlO_2^-}}\gamma_{\mathrm{AlO_2^-}}}{c_{\mathrm{H_2O}}\gamma_{\mathrm{H_2O}}}\right]\\
&+ 2K_{\mathrm{H_3SiO_4^-}}^{-1}\gamma_{\mathrm{H_3SiO_4^-}}^{-1}\left[\frac{c_{\mathrm{H_2O}}^2\gamma_{\mathrm{H_2O}}^2\cdot c_{\mathrm{SiO_2(aq)}}\gamma_{\mathrm{SiO_2(aq)}}}{c_{\mathrm{H^+}}\gamma_{\mathrm{H^+}}}\right]
\end{aligned} \tag{A.19}$$

$$\begin{aligned}
C_{\mathrm{H^+}} = {} & c_{\mathrm{H^+}} + K^{-1}_{\mathrm{CO_2(aq)}}\gamma^{-1}_{\mathrm{CO_2(aq)}}\left[\frac{c_{\mathrm{H^+}}\gamma_{\mathrm{H^+}}\cdot c_{\mathrm{HCO_3^-}}\gamma_{\mathrm{HCO_3^-}}}{c_{\mathrm{H_2O}}\gamma_{\mathrm{H_2O}}}\right] \\
& - K^{-1}_{\mathrm{OH^-}}\gamma^{-1}_{\mathrm{OH^-}}\left[\frac{c_{\mathrm{H_2O}}\gamma_{\mathrm{H_2O}}}{c_{\mathrm{H^+}}\gamma_{\mathrm{H^+}}}\right] \\
& - K^{-1}_{\mathrm{CaOH^+}}\gamma^{-1}_{\mathrm{CaOH^+}}\left[\frac{c_{\mathrm{Ca^{2+}}}\gamma_{\mathrm{Ca^{2+}}}\cdot c_{\mathrm{H_2O}}\gamma_{\mathrm{H_2O}}}{c_{\mathrm{H^+}}\gamma_{\mathrm{H^+}}}\right] \\
& - K^{-1}_{\mathrm{CaCO_3(aq)}}\gamma^{-1}_{\mathrm{CaCO_3(aq)}}\left[\frac{c_{\mathrm{Ca^{2+}}}\gamma_{\mathrm{Ca^{2+}}}\cdot c_{\mathrm{HCO_3^-}}\gamma_{\mathrm{HCO_3^-}}}{c_{\mathrm{H^+}}\gamma_{\mathrm{H^+}}}\right] \\
& - K^{-1}_{\mathrm{CO_3^{2-}}}\gamma^{-1}_{\mathrm{CO_3^{2-}}}\left[\frac{c_{\mathrm{HCO_3^-}}\gamma_{\mathrm{HCO_3^-}}}{c_{\mathrm{H^+}}\gamma_{\mathrm{H^+}}}\right] \\
& + 4K^{-1}_{\mathrm{Al^{3+}}}\gamma^{-1}_{\mathrm{Al^{3+}}}\left[\frac{c^4_{\mathrm{H^+}}\gamma^4_{\mathrm{H^+}}\cdot c_{\mathrm{AlO_2^-}}\gamma_{\mathrm{AlO_2^-}}}{c^2_{\mathrm{H_2O}}\gamma^2_{\mathrm{H_2O}}}\right] \\
& + K^{-1}_{\mathrm{HAlO_2(aq)}}\gamma^{-1}_{\mathrm{HAlO_2(aq)}}\left[\frac{c_{\mathrm{H^+}}\gamma_{\mathrm{H^+}}\cdot c_{\mathrm{AlO_2^-}}\gamma_{\mathrm{AlO_2^-}}}{1}\right] \\
& + 3K^{-1}_{\mathrm{AlOH^{2+}}}\gamma^{-1}_{\mathrm{AlOH^{2+}}}\left[\frac{c^3_{\mathrm{H^+}}\gamma^3_{\mathrm{H^+}}\cdot c_{\mathrm{AlO_2^-}}\gamma_{\mathrm{AlO_2^-}}}{c_{\mathrm{H_2O}}\gamma_{\mathrm{H_2O}}}\right] \\
& + 2K^{-1}_{\mathrm{Al(OH)_2^+}}\gamma^{-1}_{\mathrm{Al(OH)_2^+}}\left[\frac{c^2_{\mathrm{H^+}}\gamma^2_{\mathrm{H^+}}\cdot c_{\mathrm{AlO_2^-}}\gamma_{\mathrm{AlO_2^-}}}{1}\right] \\
& + K^{-1}_{\mathrm{Al(OH)_3(aq)}}\gamma^{-1}_{\mathrm{Al(OH)_3(aq)}}\left[\frac{c_{\mathrm{H^+}}\gamma_{\mathrm{H^+}}\cdot c_{\mathrm{AlO_2^-}}\gamma_{\mathrm{AlO_2^-}}}{c_{\mathrm{H_2O}}\gamma_{\mathrm{H_2O}}}\right] \\
& - K^{-1}_{\mathrm{H_3SiO_4^-}}\gamma^{-1}_{\mathrm{H_3SiO_4^-}}\left[\frac{c^2_{\mathrm{H_2O}}\gamma^2_{\mathrm{H_2O}}\cdot c_{\mathrm{SiO_2(aq)}}\gamma_{\mathrm{SiO_2(aq)}}}{c_{\mathrm{H^+}}\gamma_{\mathrm{H^+}}}\right]
\end{aligned} \tag{A.20}$$

$$\begin{aligned}
C_{\mathrm{Ca^{2+}}} = {} & c_{\mathrm{Ca^{2+}}} + K^{-1}_{\mathrm{CaHCO_3^-}}\gamma^{-1}_{\mathrm{CaHCO_3^-}}\left[\frac{c_{\mathrm{HCO_3^-}}\gamma_{\mathrm{HCO_3^-}}\cdot c_{\mathrm{Ca^{2+}}}\gamma_{\mathrm{Ca^{2+}}}}{1}\right] \\
& + K^{-1}_{\mathrm{CaOH^+}}\gamma^{-1}_{\mathrm{CaOH^+}}\left[\frac{c_{\mathrm{Ca^{2+}}}\gamma_{\mathrm{Ca^{2+}}}\cdot c_{\mathrm{H_2O}}\gamma_{\mathrm{H_2O}}}{c_{\mathrm{H^+}}\gamma_{\mathrm{H^+}}}\right] \\
& + K^{-1}_{\mathrm{CaCO_3(aq)}}\gamma^{-1}_{\mathrm{CaCO_3(aq)}}\left[\frac{c_{\mathrm{Ca^{2+}}}\gamma_{\mathrm{Ca^{2+}}}\cdot c_{\mathrm{HCO_3^-}}\gamma_{\mathrm{HCO_3^-}}}{c_{\mathrm{H^+}}\gamma_{\mathrm{H^+}}}\right]
\end{aligned} \tag{A.21}$$

$$\begin{aligned}
C_{\mathrm{HCO_3^-}} = {} & c_{\mathrm{HCO_3^-}} + K^{-1}_{\mathrm{CO_2(aq)}}\gamma^{-1}_{\mathrm{CO_2(aq)}}\left[\frac{c_{\mathrm{H^+}}\gamma_{\mathrm{H^+}}\cdot c_{\mathrm{HCO_3^-}}\gamma_{\mathrm{HCO_3^-}}}{c_{\mathrm{H_2O}}\gamma_{\mathrm{H_2O}}}\right] \\
& + K^{-1}_{\mathrm{CO_3^{2-}}}\gamma^{-1}_{\mathrm{CO_3^{2-}}}\left[\frac{c_{\mathrm{HCO_3^-}}\gamma_{\mathrm{HCO_3^-}}}{c_{\mathrm{H^+}}\gamma_{\mathrm{H^+}}}\right] \\
& + K^{-1}_{\mathrm{CaCO_3(aq)}}\gamma^{-1}_{\mathrm{CaCO_3(aq)}}\left[\frac{c_{\mathrm{Ca^{2+}}}\gamma_{\mathrm{Ca^{2+}}}\cdot c_{\mathrm{HCO_3^-}}\gamma_{\mathrm{HCO_3^-}}}{c_{\mathrm{H^+}}\gamma_{\mathrm{H^+}}}\right] \\
& + K^{-1}_{\mathrm{CaHCO_3^-}}\gamma^{-1}_{\mathrm{CaHCO_3^-}}\left[\frac{c_{\mathrm{HCO_3^-}}\gamma_{\mathrm{HCO_3^-}}\cdot c_{\mathrm{Ca^{2+}}}\gamma_{\mathrm{Ca^{2+}}}}{1}\right]
\end{aligned} \tag{A.22}$$

$$\begin{aligned}
C_{\mathrm{AlO_2^-}} = {} & c_{\mathrm{AlO_2^-}} + K^{-1}_{\mathrm{Al^{3+}}}\gamma^{-1}_{\mathrm{Al^{3+}}}\left[\frac{c^4_{\mathrm{H^+}}\gamma^4_{\mathrm{H^+}}\cdot c_{\mathrm{AlO_2^-}}\gamma_{\mathrm{AlO_2^-}}}{c^2_{\mathrm{H_2O}}\gamma^2_{\mathrm{H_2O}}}\right] \\
& + K^{-1}_{\mathrm{HAlO_2(aq)}}\gamma^{-1}_{\mathrm{HAlO_2(aq)}}\left[\frac{c_{\mathrm{H^+}}\gamma_{\mathrm{H^+}}\cdot c_{\mathrm{AlO_2^-}}\gamma_{\mathrm{AlO_2^-}}}{1}\right] \\
& + K^{-1}_{\mathrm{AlOH^{2+}}}\gamma^{-1}_{\mathrm{AlOH^{2+}}}\left[\frac{c^3_{\mathrm{H^+}}\gamma^3_{\mathrm{H^+}}\cdot c_{\mathrm{AlO_2^-}}\gamma_{\mathrm{AlO_2^-}}}{c_{\mathrm{H_2O}}\gamma_{\mathrm{H_2O}}}\right] \\
& + K^{-1}_{\mathrm{Al(OH)_2^+}}\gamma^{-1}_{\mathrm{Al(OH)_2^+}}\left[\frac{c^2_{\mathrm{H^+}}\gamma^2_{\mathrm{H^+}}\cdot c_{\mathrm{AlO_2^-}}\gamma_{\mathrm{AlO_2^-}}}{1}\right] \\
& + K^{-1}_{\mathrm{Al(OH)_3(aq)}}\gamma^{-1}_{\mathrm{Al(OH)_3(aq)}}\left[\frac{c_{\mathrm{H^+}}\gamma_{\mathrm{H^+}}\cdot c_{\mathrm{AlO_2^-}}\gamma_{\mathrm{AlO_2^-}}}{c_{\mathrm{H_2O}}\gamma_{\mathrm{H_2O}}}\right]
\end{aligned} \tag{A.23}$$

$$C_{\mathrm{SiO_2(aq)}} = c_{\mathrm{SiO_2(aq)}} + K^{-1}_{\mathrm{H_3SiO_4^-}}\gamma^{-1}_{\mathrm{H_3SiO_4^-}}\left[\frac{c^2_{\mathrm{H_2O}}\gamma^2_{\mathrm{H_2O}}\cdot c_{\mathrm{SiO_2(aq)}}\gamma_{\mathrm{SiO_2(aq)}}}{c_{\mathrm{H^+}}\gamma_{\mathrm{H^+}}}\right] \tag{A.24}$$

The mass fraction of primary chemical species can be calculated from their concentrations:

$$X^{\kappa} = \frac{C^{\kappa}M^{\kappa}}{\rho_{\mathrm{l}}} \quad \kappa = 1, \ldots, N_C \tag{A.25}$$

Then, the fluid and heat flow, solute transport, geomechanics and geochemistry during CO_2 sequestration will be simulated in the fully coupled numerical model. The geochemical system is a kinetic reaction system (H_2O(l)-CO_2(g)-$CaCO_3$(s)-Al_2 Si_2 $O_5(OH)_4$(s)- Ca(Al_2 Si_2 O_8) (s)), including the equilibrium and kinetic reactions among three phases. Geochemical reactions are fully accounted for by including speciation in the aqueous phase, CO_2 gas and calcite dissolutions into the aqueous phase, and kaolinite and anorthite dissolution/precipitation into aqueous phase. All of the potential chemical reactions occurring in aqueous phase are set to be equilibrium. The six primary aqueous species (H_2O, H^+, HCO_3^-, Ca^{2+}, SiO_2 and AlO_2^-), one primary gaseous species (CO_2(g)) and three primary mineral species ($CaCO_3$(s), Al_2 Si_2 $O_5(OH)_4$(s), and Ca(Al_2 Si_2 O_8) (s)) have been selected to dominate this chemical reaction system, there should be nine equations, of which seven mass balance equations for all the primary chemical species, one gas saturation index equation to solve dissolution concentration of CO_2 gas, and one mineral saturation index equation to solve dissolution concentration of $CaCO_3$(s). In addition, one energy balance equation is to solve temperature, and one momentum balance equation to solve mean stress. Therefore, the equation system includes eleven main equations which can represent the THMC system (CO_2 dissolution + calcite dissolution + Kaolinite dissolution/precipitation + anorthite dissolution/precipitation) numerically. The equation system is given by Eqs. A.26 – A.36.

$$\nabla\cdot\left\{\rho_{\mathrm{l}}X_{\mathrm{l}}^{\mathrm{H_2O}}\frac{KK_{rl}}{\mu_{\mathrm{l}}}(\nabla P_{\mathrm{l}} - \rho_{\mathrm{l}}g\nabla z)\right\} + \frac{\partial}{\partial t}\left\{\phi S_{\mathrm{l}}\rho_{\mathrm{l}}X_{\mathrm{l}}^{\mathrm{H_2O}}\right\} + R^{\mathrm{H_2O}} = 0 \tag{A.26}$$

$$\nabla\cdot\left\{\rho_{\mathrm{l}}X_{\mathrm{l}}^{\mathrm{H^+}}\frac{KK_{rl}}{\mu_{\mathrm{l}}}(\nabla P_{\mathrm{l}} - \rho_{\mathrm{l}}g\nabla z)\right\} + \frac{\partial}{\partial t}\left\{\phi S_{\mathrm{l}}\rho_{\mathrm{l}}X_{\mathrm{l}}^{\mathrm{H^+}}\right\} + R^{\mathrm{H^+}} = 0 \tag{A.27}$$

$$\nabla\cdot\left\{\rho_{\mathrm{l}}X_{\mathrm{l}}^{\mathrm{HCO_3^-}}\frac{KK_{rl}}{\mu_{\mathrm{l}}}(\nabla P_{\mathrm{l}} - \rho_{\mathrm{l}}g\nabla z)\right\} + \frac{\partial}{\partial t}\left\{\phi S_{\mathrm{l}}\rho_{\mathrm{l}}X_{\mathrm{l}}^{\mathrm{HCO_3^-}}\right\} + R^{\mathrm{HCO_3^-}} = 0 \tag{A.28}$$

$$\nabla\cdot\left\{\rho_{\mathrm{l}}X_{\mathrm{l}}^{\mathrm{Ca^{2+}}}\frac{KK_{rl}}{\mu_{\mathrm{l}}}(\nabla P_{\mathrm{l}} - \rho_{\mathrm{l}}g\nabla z)\right\} + \frac{\partial}{\partial t}\left\{\phi S_{\mathrm{l}}\rho_{\mathrm{l}}X_{\mathrm{l}}^{\mathrm{Ca^{2+}}}\right\} + R^{\mathrm{Ca^{2+}}} = 0 \tag{A.29}$$

$$\nabla\cdot\left\{\rho_{\mathrm{l}}X_{\mathrm{l}}^{\mathrm{SiO_2}}\frac{KK_{rl}}{\mu_{\mathrm{l}}}(\nabla P_{\mathrm{l}} - \rho_{\mathrm{l}}g\nabla z)\right\} + \frac{\partial}{\partial t}\left\{\phi S_{\mathrm{l}}\rho_{\mathrm{l}}X_{\mathrm{l}}^{\mathrm{SiO_2}}\right\} + R^{\mathrm{SiO_2}} = 0 \tag{A.30}$$

$$\nabla\cdot\left\{\rho_{\mathrm{l}}X_{\mathrm{l}}^{\mathrm{AlO_2^-}}\frac{KK_{rl}}{\mu_{\mathrm{l}}}(\nabla P_{\mathrm{l}} - \rho_{\mathrm{l}}g\nabla z)\right\} + \frac{\partial}{\partial t}\left\{\phi S_{\mathrm{l}}\rho_{\mathrm{l}}X_{\mathrm{l}}^{\mathrm{AlO_2^-}}\right\} + R^{\mathrm{AlO_2^-}} = 0 \tag{A.31}$$

$$\nabla\cdot\left\{\rho_g X_g^{CO_2}\frac{KK_{rg}}{\mu_g}\left(\nabla P_g-\rho_g g\nabla z\right)\right\}+\frac{\partial}{\partial t}\left\{\phi S_g\rho_g X_g^{CO_2}\right\}+R^{CO_2}+q_{CO_2}=0 \tag{A.32}$$

$$F_g=\log\Omega_g=\log\left[\Gamma_g^{-1}P_g^{-1}K_g^{-1}\frac{c_{H^+}\gamma_{H^+}c_{HCO_3^-}\gamma_{HCO_3^-}}{c_{H_2O}\gamma_{H_2O}}\right]=0 \tag{A.33}$$

$$F_m=\log\Omega_m=\log\left[X_m^{-1}\lambda_m^{-1}K_m^{-1}\frac{c_{Ca^{2+}}\gamma_{Ca^{2+}}c_{HCO_3^-}\gamma_{HCO_3^-}}{c_{H^+}\gamma_{H^+}}\right]=0 \tag{A.34}$$

$$\sum_\beta\nabla\cdot\left\{h_\beta\rho_\beta\frac{KK_{r\beta}}{\mu_\beta}\left(\nabla P_\beta-\rho_\beta g\nabla z\right)\right\}-\lambda\nabla T+\frac{\partial U}{\partial t}=0 \tag{A.35}$$

$$\frac{3(1-v)}{1+v}\nabla\tau-\frac{2(1-2v)}{1+v}(\alpha\nabla p+3\beta K\nabla T)+\overline{F}=0 \tag{A.36}$$

In the equation system of this THMC model (CO_2 dissolution + calcite dissolution + Kaolinite dissolution/precipitation + anorthite dissolution/precipitation) for CO_2 injection, seven mass balance equations are present for six primary aqueous chemical species (H_2O, H^+, HCO_3^-, Ca^{2+}, SiO_2 and AlO_2^-) and one primary gaseous chemical species ($CO_2(g)$). Every mass balance equation has a generation term (R) due to mass gain or loss by chemical reaction between different phases, especially mineral dissolution and precipitation, which are under equilibrium or kinetic condition. Therefore, the source or sink term due to chemical reaction can be expressed mathematically as follows.

$$R^{H_2O}=-c_{CO_2(g)}+r_{Al_2Si_2O_5(OH)_4(s)}\Delta t \tag{A.37}$$

$$R^{H^+}=c_{CO_2(g)}-c_{CaCO_3(s)}+2r_{Al_2Si_2O_5(OH)_4(s)}\Delta t \tag{A.38}$$

$$R^{HCO_3^-}=c_{CO_2(g)}+c_{CaCO_3(s)} \tag{A.39}$$

$$R^{Ca^{2+}}=c_{CaCO_3(s)}+r_{Ca(Al_2Si_2O_8)(s)}\Delta t \tag{A.40}$$

$$R^{SiO_2}=2r_{Al_2Si_2O_5(OH)_4(s)}\Delta t+2r_{Ca(Al_2Si_2O_8)(s)}\Delta t \tag{A.41}$$

$$R^{AlO_2^-}=2r_{Al_2Si_2O_5(OH)_4(s)}\Delta t+2r_{Ca(Al_2Si_2O_8)(s)}\Delta t \tag{A.42}$$

$$R^{CO_2}=c_{CO_2(g)} \tag{A.43}$$

Eleven unknown variables are selected as the primary variable for the fully coupled reactive solute transport model, i.e., P, c_{H^+}, $c_{HCO_3^-}$, $c_{Ca^{2+}}$, c_{SiO_2}, $c_{AlO_2^-}$, S_g, $c_{CO_2(g)}$, $c_{CaCO_3(s)}$, T and τ. Newton–Raphson iteration method is used to solve the equation system of the fully coupled reactive solute transport model. The numerical derivatives of mass balance equations by each primary variable forms Jacobian matrix of the equation system. The incident matrix of one grid cell is taken as an example to illustrate the Jacobian matrix setup, which is shown in Eq. (A.44).

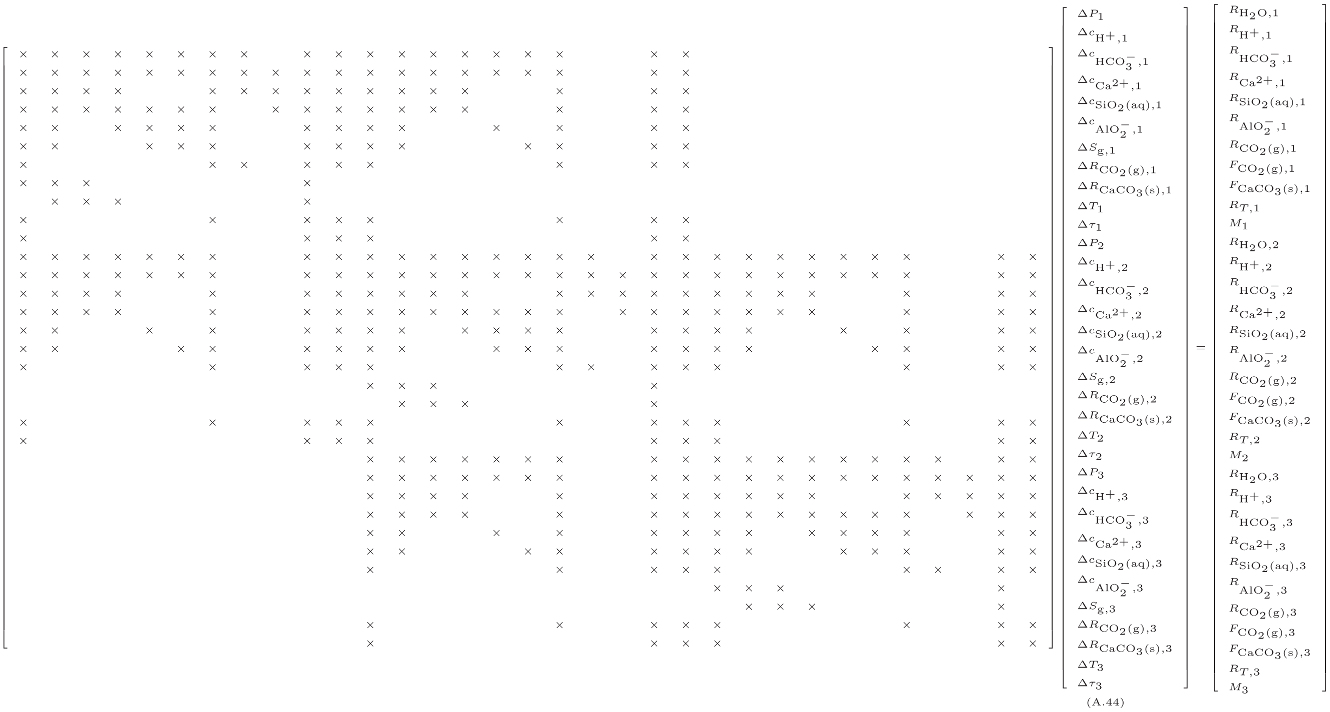

(A.44)

References

Ague, J.J., Brimhall, G.H., 1989. Geochemical modeling of steady state fluid flow and chemical reaction during supergene enrichment of porphyry copper deposits. Econ. Geol. 84 (3), 506–528. http://economicgeology.org/content/84/3/506.abstract.

Appelo, C.A.J., 1994. Cation and proton exchange, ph variations, and carbonate reactions in a freshening aquifer. Water Resour. Res. 30 (10), 2793–2805. http://dx.doi.org/10.1029/94WR01048.

Bear, J., 1972. Dynamics of Fluids in Porous Media. American Elsevier.

Bethke, C.M., 2002. The Geochemists Workbench Release 4.0: a Users Guide to Rxn, Act2, Tact, React, and Gtplot.

Busch, A., Kampman, N., Hangx, S., Snippe, J., Bickle, M., Bertier, P., Chapman, H., Spiers, C., Pijnenburg, R., Samuelson, J., Evans, J., Maskell, A., Nicholl, J., Pipich, V., Di, Z., Rother, G., Schaller, M., 2014. The green river natural analogue as a field laboratory to study the long-term fate of {CO2} in the subsurface. Energy Procedia 63, 2821–2830, 12th International Conference on Greenhouse Gas Control Technologies, GHGT-12. http://www.sciencedirect.com/science/article/pii/S1876610214021195.

Cederberg, G.A., Street, R.L., Leckie, J.O., 1985. A groundwater mass transport and equilibrium chemistry model for multicomponent systems. Water Resour. Res. 21 (8), 1095–1104. http://dx.doi.org/10.1029/WR021i008p01095.

Corey, A.T., 1954. The interrelation between gas and oil relative permeabilities. Prod. Mon. 19 (1), 38–41.

Davies, J.P., Davies, D.K., 2001. Stress-dependent permeability: characterization and modeling. SPE J. 6 (2), 224–235.

Delshad, M., Pope, G.A., Sepehrnoori, K., 1996. A compositional simulator for modeling surfactant enhanced aquifer remediation, 1 formulation. J. Contam. Hydrol. 23 (4), 303–327. http://www.sciencedirect.com/science/article/pii/0169772295001069.

Engesgaard, P., Kipp, K.L., 1992. A geochemical transport model for redox-controlled movement of mineral fronts in groundwater flow systems: a case of nitrate removal by oxidation of pyrite. Water Resour. Res. 28 (10), 2829–2843. http://dx.doi.org/10.1029/92WR01264.

Feely, R.A., Sabine, C.L., Lee, K., Berelson, W., Kleypas, J., Fabry, V.J., Millero, F.J., 2004. Impact of anthropogenic co_2 on the $caco_3$ system in the oceans. Science 305 (5682), 362–366. http://www.sciencemag.org/content/305/5682/362.abstract.

Guimarães, L.D.N., Gens, A., Olivella, S., 2007. Coupled thermo-hydro-mechanical and chemical analysis of expansive clay subjected to heating and hydration. Transp. Porous Media 66 (3), 341–372.

Hangx, S., Bakker, E., Bertier, P., Nover, G., Busch, A., 2015. Chemical mechanical coupling observed for depleted oil reservoirs subjected to long-term co2-exposure a case study of the werkendam natural {CO2} analogue field. Earth Planet. Sci. Lett. 428, 230–242. http://www.sciencedirect.com/science/article/pii/S0012821X15004793.

Hitchon, B., 1996. Aquifer Disposal of Carbon Dioxide: Hydrodynamic and Mineral Trapping: Proof of Concept. Geoscience Pub.

IPCC, 2005. IPCC Special Report on Carbon Dioxide Capture and Storage. Cambridge University Press, New York, NY, USA.

IPCC, 2007. Climate Change 2007: the Physical Science Basis. Contribution of Working Group I to the Fourth Assessment Report of the Intergovernmental Panel on Climate Change. Cambridge University Press, Cambridge, United Kingdom and New York, NY, USA.

Kharaka, Y.K., Gunter, W.D., Aggarwal, P.K., Perkins, E.H., DeBraal, J.D., 1989. SOLMINEQ. 88: a Computer Program for Geochemical Modeling of Water-rock Interactions. US Geological Survey Menlo Park, California.

Kohl, T., Evansi, K., Hopkirk, R., Rybach, L., 1995. Coupled hydraulic, thermal and mechanical considerations for the simulation of hot dry rock reservoirs. Geothermics 24 (3), 345–359.

Lasaga, A.C., 1984. Chemical kinetics of water-rock interactions. J. Geophys. Res. 89 (B6), 4009–4025.

Lasaga, A.C., Soler, J.M., Ganor, J., Burch, T.E., Nagy, K.L., 1994. Chemical weathering rate laws and global geochemical cycles. Geochim. Cosmochim. Acta 58 (10), 2361–2386.

Liu, C.W., Narasimhan, T.N., 1989. Redox-controlled multiple-species reactive chemical transport: 1. model development. Water Resour. Res. 25 (5), 869–882. http://dx.doi.org/10.1029/WR025i005p00869.

Longuemare, P., Mainguy, M., Lemonnier, P., Onaisi, A., Gérard, C., Koutsabeloulis, N., 2002. Geomechanics in reservoir simulation: overview of coupling methods and field case study. Oil Gas Sci. Technol. 57 (5), 471–483.

Marbler, H., Erickson, K.P., Schmidt, M., Lempp, C., Pöllmann, H., 2013. Geomechanical and geochemical effects on sandstones caused by the reaction with supercritical co2: an experimental approach to in situ conditions in deep geological reservoirs. Environ. Earth Sci. 69 (6), 1981–1998.

McKee, C.R., Bumb, A.C., Koenig, R.A., 1988. Stress-dependent permeability and porosity of coal and other geologic formations. SPE Form. Eval. 3 (1), 81–91.

Minkoff, S.E., Stone, C.M., Bryant, S., Peszynska, M., Wheeler, M.F., 2003. Coupled fluid flow and geomechanical deformation modeling. J. Pet. Sci. Eng. 38 (1), 37–56.

Najafabadi, N.F., Han, C., Delshad, M., Sepehrnoori, K., 2009. Development of a three phase, fully implicit, parallel chemical flood simulator. SPE 119002. In: SPE Reservoir Simulation Symposium, 2–4 February 2009, The Woodlands, Texas.

Nguyen, T., 1996. Description of the computer code fracon. Dev. Geotech. Eng. 79, 539–544.

Noorishad, J., Tsang, C.F., Witherspoon, P.A., 1984. Coupled thermal-hydraulic-mechanical phenomena in saturated fractured porous rocks: numerical approach. J. Geophys. Res. Solid Earth (1978–2012) 89 (B12), 10365–10373.

Orr, J.C., Fabry, V.J., Aumont, O., Bopp, L., Doney, S.C., Feely, R.A., Gnanadesikan, A., Gruber, N., Ishida, A., Joos, F., Key, R.M., Lindsay, K., Maier-Reimer, E., Matear, R., Monfray, P., Mouchet, A., Najjar, R.G., Plattner, G.K., Rodgers, K.B., Sabine, C.L., Sarmiento, J.L., Schlitzer, R., Slater, R.D., Totterdell, I.J., Weirig, M.F., Yamanaka, Y., Yool, A., 2005. Anthropogenic ocean acidification over the twenty-first century and its impact on calcifying organisms. Nature 437 (7059), 681–686.

Ostensen, R.W., 1986. The effect of stress-dependent permeability on gas production and well testing. SPE Form. Eval. 1 (3), 227–235.

Palandri, J.L., Kharaka, Y.K., 2004. A Compilation of Rate Parameters of Water-mineral Interaction Kinetics for Application to Geochemical Modeling. Tech. rep., no. OPEN-FILE-2004-1068. Geological Survey, Menlo Park, Californial.

Parkhurst, D.L., Appelo, C.A.J., et al., 1999. User's Guide to PHREEQC (Version 2): a Computer Program for Speciation, Batch-reaction, One-dimensional Transport, and Inverse Geochemical Calculations.

Parkhurst, D.L., Thorstenson, D.C., Plummer, L.N., 1991. Phreeque: a computer program for geochemical calculations—us geological survey. Water Resour. Investig. 80–90.

Rutqvist, J., Tsang, C., 2002. A study of caprock hydromechanical changes associated with co_2-injection into a brine formation. Environ. Geol. 42 (2–3), 296–305.

Rutqvist, J., Wu, Y.-S., Tsang, C.-F., Bodvarsson, G., 2002. A modeling approach for analysis of coupled multiphase fluid flow, heat transfer, and deformation in fractured porous rock. Int. J. Rock Mech. Min. Sci. 39 (4), 429–442.

Samier, P., Onaisi, A., de Gennaro, S., et al., 2008. A practical iterative scheme for coupling geomechanics with reservoir simulation. SPE Reserv. Eval. Eng. 11 (05), 892–901.

Settari, A., Walters, D.A., et al., 2001. Advances in coupled geomechanical and reservoir modeling with applications to reservoir compaction. SPE J. 6 (03), 334–342.

Šimůnek, J., Suarez, D.L., 1994. Two-dimensional transport model for variably saturated porous media with major ion chemistry. Water Resour. Res. 30 (4), 1115–1133. http://dx.doi.org/10.1029/93WR03347.

Steefel, C.I., Lasaga, A.C., 1994. A coupled model for transport of multiple chemical species and kinetic precipitation/dissolution reactions with application to reactive flow in single phase hydrothermal systems. Am. J. Sci. 294 (5), 529–592.

Szulczewski, M.L., MacMinn, C.W., Herzog, H.J., Juanes, R., 2012. Lifetime of carbon capture and storage as a climate-change mitigation technology. Proc. Natl. Acad. Sci. 109 (14), 5185–5189.

Tran, D., Settari, A., Nghiem, L., et al., 2004. New iterative coupling between a reservoir simulator and a geomechanics module. SPE J. 9 (03), 362–369.

Van Genuchten, M.T., 1980. A closed-form equation for predicting the hydraulic conductivity of unsaturated soils. Soil Sci. Soc. Am. J. 44 (5), 892–898.

Verma, A., Pruess, K., 1988. Thermohydrological conditions and silica redistribution near high-level nuclear wastes emplaced in saturated geological formations. J. Geophys. Res. Solid Earth (1978–2012) 93 (B2), 1159–1173.

Walter, A.L., Frind, E.O., Blowes, D.W., Ptacek, C.J., Molson, J.W., 1994. Modeling of multicomponent reactive transport in groundwater: 2. metal mobility in aquifers impacted by acidic mine tailings discharge. Water Resour. Res. 30 (11), 3149–3158. http://dx.doi.org/10.1029/94WR00954.

Wang, W., Kolditz, O., 2007. Object-oriented finite element analysis of thermo-hydro-mechanical (thm) problems in porous media. Int. J. Numer. Methods Eng. 69 (1), 162–201.

Wei, L., 2012. Sequential coupling of geochemical reactions with reservoir simulations for waterflood and eor studies. SPE J. 30 (6), 469–484.

Winterfeld, P.H., Wu, Y., 2012. A novel fully coupled geomechanical model for co_2 sequestration in fractured and porous brine aquifers. In: XIX International Conference on Water Resources CMWR, pp. 17–22.

Winterfeld, P.H., Wu, Y., Pruess, K., Oldenburg, C., 2012. Development of an advanced thermal-hydraulic-mechanical model for co_2 storage in porous and fractured saline aquifers. In: Proceedings, TOUGH Symposium 2012Lawrence Berkeley National Laboratory, Berkeley, California, September 17–19, 2012.

Wolery, T.J., 1992. EQ3/6: a Software Package for Geochemical Modeling of Aqueous Systems: Package Overview and Installation Guide (Version 7.0). Lawrence Livermore National Laboratory Livermore, CA.

Wu, Y.-S., Chen, Z., Kazemi, H., Yin, X., Pruess, K., Oldenburg, C., Winterfeld, P., Zhang, R., 2014. Simulation of Coupled Processes of Flow, Transport, and Storage of Co_2 in Saline Aquifers. In: Tech. Rep.. Trustees Of The Colorado School Of Mines. http://www.osti.gov/scitech/servlets/purl/1167349.

Xiong, Y., Fakcharoenphol, P., Winterfeld, P.H., Zhang, R., Wu, Y.-S., 2013. Coupled geomechanical and reactive geochemical model for fluid and heat flow: application for enhanced geothermal reservoir. In: SPE Reservoir Characterization and Simulation Conference and Exhibition, 16–18 September. UAE. SPE, Abu Dhabi.

Xu, T., 1996. Modeling Non-isothermal Multicomponent Reactive Solute Transport through Variably Saturated Porous Media (Ph.D. thesis). Civil Engineering School, University of La Coruña, Coruña, Spain.

Xu, T., Gérard, F., Pruess, K., Brimhall, G., 1997. Modeling Non-isothermal Multiphase Multi-species Reactive Chemical Transport in Geologic Media. Tech. rep., Lawrence Livermore National Lab, CA, United States.

Xu, T., Sonnenthal, E., Spycher, N., k, P., 2004. Toughreact Users Guide: a Simulation Program for Nonisothermal Multiphase Reactive Geochemical Transport in

Variably Saturated Geologic Media. Lawrence Berkeley National Laboratory, Berkeley, California.

Xu, T., Sonnenthal, E., Spycher, N., Pruess, K., 2006. Toughreact-a simulation program for non-isothermal multiphase reactive geochemical transport in variably saturated geologic media: applications to geothermal injectivity and co_2 geological sequestration. Comput. Geosci. 32 (2), 145–165.

Yao, Y., Wu, Y.-S., Zhang, R., 2012. The transient flow analysis of fluid in a fractal, double-porosity reservoir. Transp. Porous Media 94 (1), 175–187.

Yeh, G.T., Tripathi, V.S., 1991. A model for simulating transport of reactive multispecies components: model development and demonstration. Water Resour. Res. 27 (12), 3075–3094. http://dx.doi.org/10.1029/91WR02028.

Zhang, R., 2013. Numerical Simulation of Thermal Hydrological Mechanical Chemical Processes during Co_2 Geological Sequestration (Ph.D. thesis). Colorado School of Mines.

Zhang, R., Winterfeld, P.H., Yin, X., Xiong, Y., Wu, Y.-S., 2015. Sequentially coupled thmc model for co 2 geological sequestration into a 2d heterogeneous saline aquifer. J. Nat. Gas Sci. Eng.

Zhang, R., Wu, Y.-S., Fakcharoenphol, P., 2014. Non-darcy displacement in linear composite and radial aquifer during co2 sequestration. Int. J. Oil Gas Coal Technol. 7 (3), 244–262.

Zhang, R., Yin, X., Winterfeld, P.H., Wu, Y.-S., 2012a. A fully coupled model of nonisothermal multiphase flow, geomechanics, and chemistry during co_2 sequestration in brine aquifers. In: Proceedings of the TOUGH Symposium, pp. 838–848.

Zhang, R., Yin, X., Wu, Y.-S., Winterfeld, P.H., 2012b. A fully coupled model of nonisothermal multiphase flow, solute transport and reactive chemistry in porous media. In: SPE Annual Technical Conference and Exhibition, 8–10 October, San Antonio, Texas, USA.

Zhao, X., Rui, Z., Liao, X., Zhang, R., 2015a. The qualitative and quantitative fracture evaluation methodology in shale gas reservoir. J. Nat. Gas Sci. Eng.

Zhao, X., Rui, Z., Liao, X., Zhang, R., 2015b. A simulation method for modified isochronal well testing to determine shale gas well productivity. J. Nat. Gas Sci. Eng.

Zheng, L., Rutqvist, J., Birkholzer, J.T., Liu, H.-H., 2015. On the impact of temperatures up to 200 c in clay repositories with bentonite engineer barrier systems: a study with coupled thermal, hydrological, chemical, and mechanical modeling. Eng. Geol. 197, 278–295.

Zheng, L., Samper, J., 2008. A coupled thmc model of febex mock-up test. Phys. Chem. Earth Parts A/B/C 33, S486–S498.

Zysset, A., Stauffer, F., Dracos, T., 1994. Modeling of reactive groundwater transport governed by biodegradation. Water Resour. Res. 30 (8), 2423–2434. http://dx.doi.org/10.1029/94WR01045.